Advances in Water Resources 187 (2024) 104688

Contents lists available at ScienceDirect

Advances in Water Resources

journal homepage: www.elsevier.com/locate/advwatres

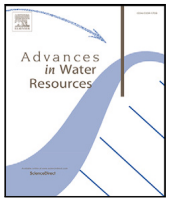

Ostwald ripening of gas bubbles in porous media: Impact of pore geometry and spatial bubble distribution

Deepak Singh [a,*], Helmer André Friis [a], Espen Jettestuen [b], Johan Olav Helland [c]

[a] Department of Energy and Petroleum Engineering, University of Stavanger, P.O. Box 8600, N-4036 Stavanger, Norway
[b] NORCE Norwegian Research Centre, Tullins gate 2, N-0166 Oslo, Norway
[c] NORCE Norwegian Research Centre, P.O. Box 8046, N-4068 Stavanger, Norway

ARTICLE INFO

Dataset link: Ostwald ripening of gas bubbles in porous media: Impact of pore geometry and spatial bubble distribution (Original data)

Keywords:
Ostwald ripening
Pore-scale
Gas-bubble populations
Capillary trapping
Level set method

ABSTRACT

We study pore-scale gas bubble ripening in porous media by combining a mass transfer method based on chemical potential differences with a level-set method for updating the gas/liquid configurations. We examine the impact of pore geometry and initial gas bubble distribution on the evolution, as well as the effect of mesh refinement and numerical parameters controlling the adaptive time steps in the model. Our results show that the pore geometry has a significant impact as it determines the rate of bubble pressure change with volume, while the area for mass transfer influences the time scale of the evolution. Simulations with different spatial patterns of bubbles with high and low pressures yield different ripening behaviors, classified as local and global ripening regimes. Simulations on sandstone with volumetrically similar bubble distributions display different ripening paths depending on the initial bubble locations, emphasizing the importance of capturing displacement history before ripening investigations.

1. Introduction

Subsurface storage of CO_2 is one of the measures that the UN Intergovernmental Panel on Climate Change recommends to keep global warming within 1.5 °C (de Coninck et al., 2018). Although permanent mineral trapping provides the safest long-term CO_2 storage solution, it has been observed that residual trapping due to strong capillary forces can also provide a safe and stable way to store large amounts of CO_2 (Huppert and Neufeld, 2014; Pentland et al., 2011). Residual trapping occurs when brine imbibes into the pore space at the trailing edge of the migrating CO_2 plume and snaps off CO_2 ganglia (Krevor et al., 2015). Over time we could expect CO_2 ganglia to either dissolve in brine or persist if the brine is already saturated with CO_2, depending on the reservoir conditions. In the first scenario, water with dissolved CO_2 sinks below water without CO_2 (convective mixing), increasing the overall geological storage capacity (Zhang and Song, 2014). In both scenarios, if the trapping lasts a very long time (more than 10^4 years), the stored CO_2 can transform permanently into carbonate minerals (Xu et al., 2004). Determining how the population of the formed gas ganglia evolves is important in estimating the life and volume of subsurface gas stored through residual trapping.

Ostwald ripening of gas bubbles is an inter-bubble diffusion process by which low-pressure bubbles consume adjacent high-pressure bubbles (de Vries, 1958). In bulk liquid, the process leads to mass transfer from smaller to larger bubbles due to pressure differences described by the Young–Laplace effect (Stevenson, 2010). This type of growth is referred to as the ripening or coarsening of bubble-size distributions. In bulk liquid, a bubble distribution coarsens continuously as smaller bubble sizes disappear sequentially based on size (de Vries, 1958). But in porous media, the pore geometry creates local energy barriers that result in the coexistence of multiple bubble sizes at thermodynamic equilibrium (de Chalendar et al., 2017). In recent years, many studies have been conducted to assess the impact of Ostwald ripening on subsurface residually trapped CO_2 (de Chalendar et al., 2017; Xu et al., 2017, 2019; Li et al., 2020, 2021; Singh et al., 2022; Blunt, 2022; Moghadasi et al., 2023). They show that even though the process is slow, it can lead to significant mass redistribution on both the pore scale and field scale. Ripening on the pore scale is much faster than on the field scale, and the ripening rate depends on the type of gas and reservoir condition (Singh et al., 2022; Blunt, 2022). Formation of a gas cap in storage reservoirs (Xu et al., 2019), growth of bubbles in microfractures (Singh et al., 2022), and capillary instabilities (e.g., Haines jumps) (de Chalendar et al., 2017) are some of the processes that can result from coarsening of the presumed trapped bubble distribution at the different scales. Apart from its effect on subsurface CO_2 storage, the impact of Ostwald ripening on foam coarsening in bulk liquid and during enhanced oil recovery has also been widely reported and

* Corresponding author.
E-mail address: deepak.singh@uis.no (D. Singh).

https://doi.org/10.1016/j.advwatres.2024.104688
Received 20 July 2023; Received in revised form 13 March 2024; Accepted 22 March 2024
Available online 26 March 2024

studied (Lifshitz and Slyozov, 1961; Lemlich, 1978; Kim, 2007; Attia et al., 2013; Farajzadeh et al., 2014; Xue et al., 2016).

Ostwald ripening of gas bubbles at the pore scale in porous media is a complicated phenomenon. The impact of pore geometry on bubble pressures can lead to both coarsening and anti-coarsening of gas bubble distributions (de Chalendar et al., 2017; Xu et al., 2017; Singh et al., 2022). Xu et al. (2017) conducted experimental investigations of Ostwald ripening using a water-wet glass micromodel filled with trapped air and surfactant aqueous solutions. Their analysis showed that bubble distributions undergo significant mass redistribution in hours. The authors also developed a theoretical model based on their experimental results.

Modeling ripening physics at the pore scale is challenging since the coarsening behavior depends on both pore geometry and wetting state (Xu et al., 2017; Mehmani and Xu, 2022a). Generally, a numerical pore-scale model for gas bubble ripening in a stationary liquid will need to simulate two processes: interface readjustment and diffusive mass transfer through the intermediate liquid phase. Here, mass transfer is the rate-determining process (de Chalendar et al., 2017). Therefore, it is convenient to model the ripening by capillary displacement and mass transfer in alternate steps, assuming that mass transfer time represents the time for the complete ripening process.

A challenge is to model accurately the bubble distribution evolution in real pore geometries from segmented microtomography images. Pore-scale modeling of Ostwald ripening typically relies on simplifying the pore geometry into pore network models (PNM) or homogeneous systems and limiting the size of a bubble to a single pore (de Chalendar et al., 2017; Xu et al., 2017, 2019; Mehmani and Xu, 2022a). Such models require prior knowledge of capillary pressure–volume relationships for the gas bubbles in the porous structure. While this is a tractable modeling approach to ripening on idealized pore geometries, it is less suitable on real pore geometries where all pores are different. Bubble growth beyond single pores, for which the pressure–volume relationships become non-monotonic, could trigger capillary instabilities like snap-off events or Haines jumps and bubble mobilization, hence contributing significantly to the complexity of ripening modeling of bubbles spanning multiple pores. Recently, Mehmani and Xu (2022b) proposed an improved pore network model for coarsening that can accommodate multi-pore bubbles. Despite the pore geometry idealization, these models have been able to predict the bubbles' coarsening and anti-coarsening behavior observed in micromodel experiments (Xu et al., 2017; Mehmani and Xu, 2022a,b).

In a recent work (Singh et al., 2022), we presented a methodology for simulating the ripening of gas bubbles on arbitrary pore geometries. This approach uses a ghost bubble (GB) method to perform the mass transfer and a conservative level set (LS) method (Jettestuen et al., 2021) to update the stationary states of the gas/liquid configurations and calculate the gas bubble pressures. The GB method calculates the chemical potentials of imaginary ghost bubbles located in the liquid regions and uses them to distribute mass to their gas bubble neighbors based on chemical potential differences. The results highlighted that a disconnected liquid phase (which can occur for weakly wet states) also affects the ripening dynamics (Singh et al., 2022). The results confirmed that the GB method combined with the conservative LS method obeys mass conservation with negligible mass loss during evolution. The model was also used to predict the ripening of multi-pore bubbles in a pore geometry from sandstone. However, the GB method utilized an effective permeability coefficient in the mass transfer equation based on dimensional analysis that restricted the evolution to a non-dimensional time scale. Consequently, although the nature of evolution is predicted accurately, its time scale remains unknown.

Such direct simulation methods for ripening will benefit from adaptive time steps in the mass transfer to improve computational efficiency. For digital representations of the pore geometry, the resolution of the mesh and time step impacts the accuracy in the discretization of continuous mass transfers, which could lead to mass transfer cyclicity. This cyclicity is a numerical artifact where a discrete amount of mass transferred from one bubble to another in a time step is reversed in the next time step (Singh et al., 2022). It is also possible that more than two bubbles participate in such cyclicity leading to gas bubble pressure fluctuations in the vicinity of the stable state. So, the time step must be set heuristically within a user-defined range. Further complexity in determining this time step is that the bubble pressure after interface readjustment (which impacts the next mass transfer) is not known *a priori*. In such cases, the mass transfer between two bubbles at a time step could be more than the mass transfer required to reach equilibrium and thus result in a mass transfer in the reverse direction in the next time step. A limitation in our previous work (Singh et al., 2022) lies in handling mass transfer cyclicity, as the time step was calculated based on a constant, maximal bubble volume change.

In this work, we introduce another chemical-potential based method for the mass transfer, called the bubble-to-bubble (BB) method, that we also couple with the LS method for simulation of Ostwald ripening of trapped gas bubbles in arbitrary pore geometries. The main advantage of the BB method over the GB method is that it considers all effective mass transfer paths directly between the gas bubbles, which renders possible the use of theoretically derived phase permeability coefficients in the mass transfer equations based on Fick's first law of diffusion. Hence, the BB method allows simulations of gas-bubble ripening on a dimensional time scale. We use the theoretical phase permeability to derive conditions for which the GB method becomes equivalent to the BB method.

Our objective is to use the coupled BB and LS methods in simulations to investigate the impact of pore geometry and spatial bubble distribution on ripening evolution. Although previous studies have shown that pore geometry can lead to coarsening or anti-coarsening behavior (de Chalendar et al., 2017; Xu et al., 2017), the importance of pore throat geometry on the rate of this evolution needs to be studied numerically. This analysis is critical since numerical modeling of this phenomenon typically idealizes pore geometry. Similarly, the effect of initial bubble distribution on evolution in bulk foam due to Ostwald ripening has been studied by Ranadive and Lemlich (1979), but the impact of spatial patterns of trapped gas bubbles with different sizes in porous media is not fully explored (Singh et al., 2022; Mehmani and Xu, 2022a). The current work is an attempt to fill this gap in scientific knowledge. Finally, we will also evaluate the significance of using adaptive mesh in ripening simulations, as well as explore the sensitivity of numerical control parameters that determines adaptive time steps and minimum tracked gas bubble size, which is important to achieve high computational efficiency while maintaining a sufficient level of detail in the simulations.

The paper is organized as follows: Section 2 describes the methodology, including the BB, GB, and LS methods, and provides a brief outline of the combined Ostwald ripening model. Section 3 compares the calculated capillary pressure at thermodynamic equilibrium against analytical values and also substantiates the mass conservation in the models. Section 4 compares the BB method against the GB method. Section 5 explores the effects of pore geometry on ripening, using both pore-throat geometries and micromodel geometries. Section 6 presents simulations with different spatial bubble patterns in micromodel geometries and in sandstone. For simulations in sandstone, we also examine the effect of adaptive mesh refinement and numerical control parameters. Finally, Section 7 contains the summary and conclusions.

2. Methodology

Ostwald ripening of gas bubbles is a spontaneous, diffusive mass transfer process governed by the gas concentration gradient in the liquid surrounding the bubbles (de Vries, 1958; Xu et al., 2017). It transfers mass from bubbles with high chemical potential to bubbles

with low chemical potential to minimize Gibbs free energy. At thermodynamic equilibrium, the fluid system has reached a state in which the partial pressure of the gas component (and hence its chemical potential) is constant in time and space. For real gases, the chemical potential at a particular temperature T [K] is calculated as (Castellan, 1983):

$$\mu = \mu_{std} + RT \ln f \ , \tag{1}$$

where μ_{std} [J mol^{-1}] is the chemical potential of the pure gas at standard pressure (typically $P_{std} = 101,325$ Pa), R [8.314 J mol^{-1} K^{-1}] is the universal gas constant, and f is the fugacity. For ideal gases, fugacity is replaced by the pressure P [Pa] made non-dimensional by P_{std} (Castellan, 1983).

To develop the pore-scale model, we make the following assumptions: (i) Interface readjustment occurs instantaneously, and diffusive mass transfer is the only contributor to the physical time scale for the ripening (de Chalendar et al., 2017). (ii) A liquid droplet (or region) in contact with only one gas bubble is in thermodynamic equilibrium with it. This equilibrium represented by equal chemical potentials is reached spontaneously (Castellan, 1983). (iii) The mass transfer occurs due to chemical potential differences in the liquid region between two or more gas bubbles. Here, we consider mass transfer only through bulk liquid regions and neglect wetting films. (iv) Two gas bubbles interact with each other only through the liquid (de Chalendar et al., 2017). (v) There is no mass accumulation or loss (dissolution) from gas bubbles to the intermediate liquid during Ostwald ripening. Liquid regions only act as mass transfer paths between the bubbles. (vi) Reservoir temperature is constant and above the critical temperature of the gas. The last assumption simplifies calculations by ensuring that the chemical species is in one phase, i.e., gas or supercritical fluid, and phase change calculations are not required. The impact of these assumptions has been outlined by Singh et al. (2022).

The general equation for mass transfer rate ($\partial n_{ij}/\partial t$) [mol s^{-1}] governed by chemical potential differences between two gas bubbles i and j can be written as:

$$\frac{\partial n_{ij}}{\partial t} = -J A_c \Delta\mu_{ij} = -J A_c(\mu_i - \mu_j) \ , \tag{2}$$

where, J [mol^2 s kg^{-1} m^{-4}] is the effective phase permeability constant for the mass transfer, A_c [m^2] is the area through which the mass transfer occurs, and $\Delta\mu_{ij}$ is the chemical potential difference between the gas bubbles i and j. The negative sign in Eq. (2) indicates mass transfer direction from higher to lower potential. As there is no mass accumulation in the liquid (assumption (v)), $\partial n_{ij}/\partial t = -\partial n_{ji}/\partial t$.

Combining Eqs. (1) and (2) gives

$$\frac{\partial n_{ij}}{\partial t} = -(J A_c) \times (RT) \left(\ln \frac{f_i}{f_j} \right) \ . \tag{3}$$

When mass transfer paths in the surrounding liquid connect bubble i to more than one bubble, Eq. (3) describes the mass transfer between bubble i and one of its bubble neighbors j. However, the calculation of the entire mass change of bubble i will include the mass transfer contributions from all its neighbors. In this work, we describe two methods to perform these calculations (Sections 2.1 and 2.2). In the BB method, we aggregate the mass transfer through different diffusion paths linking the gas bubble i to other bubbles, while in the GB method, we aggregate the mass interaction of bubble i through the different liquid regions adjacent to it. Both methods utilize the LS method to adjust the interface positions and to calculate bubble pressures and surface areas after each mass transfer step, as described in Section 2.3. In Eq. (3), we calculate gas bubble fugacities from gas pressure and compressibility factor, using Peng–Robinson equation of state (PR EoS) (Ahmed, 2010; de Nevers, 2012) as described in supplementary information S1. In the following two subsections, we describe the methodology for determining the mass transfer rate of a bubble for BB and GB methods. In addition, Section 2.1 derives an expression for phase permeability J in the BB method that we relate to the phase permeability of the GB method in Section 2.2.

2.1. Mass transfer rate for bubble-to-bubble method

As mentioned earlier, a diffusion path linking one bubble to another bubble passes only through liquid regions (assumption iv). Since the pore geometry traps these bubbles, there can be many diffusion paths between the same bubble pair. A distinct, effective diffusion path k between two bubbles i and j is defined as the unique path that connects a gas/liquid interface of bubble i to a gas/liquid interface of bubble j. We begin by deriving a theoretical expression for J along one such path k based on the chemical potential differences in Eq. (3). As such, our derivation differs slightly from the work of Xu et al. (2017), who developed a permeability coefficient for mass transfer governed by capillary pressure differences and then validated it against micromodel experiments.

According to Fick's law of gas diffusion, the mass flux N' [kg m^{-2} s^{-1}] is:

$$N' = \frac{\rho_g}{A_c}\frac{\partial V_g}{\partial t} = -D\frac{\partial C}{\partial x} \ , \tag{4}$$

where ρ_g [kg m^{-3}] is the density of the gas, $\partial V_g/\partial t$ [m^3 s^{-1}] is the rate of change of bubble volume, A_c [m^2] is the effective area of mass transfer, and D [m^2 s^{-1}] is the diffusion coefficient of the gas in the liquid. Let M_α [kg mol^{-1}] and n_α [mol], $\alpha = g, l$, be the molar mass and number of moles of the gas (g) and liquid (l) phases, respectively. Then $C \approx (n_g M_g)/(n_l M_l/\rho_l)$ [kg m^{-3}] is the concentration of gas in the liquid with density ρ_l.

Henry's law provides a relationship between the molar ratio of dissolved gas in the liquid and the partial gas pressure (or equivalently, gas bubble pressure) P_g:

$$\frac{n_g}{n_l} = \frac{P_g}{K^{px}} \ , \tag{5}$$

where K^{px} [Pa] is Henry's volatility. If P_l is the liquid pressure and P_c is the capillary pressure between the gas bubble and liquid, then $P_g = P_l + P_c$. Using Eq. (5), we can rewrite Eq. (4) as:

$$\frac{\partial V_g}{\partial t} = -\frac{M_g \rho_l}{M_l \rho_g}\frac{D}{K^{px}} A_c \frac{\partial P_g}{\partial x} \ . \tag{6}$$

We consider a diffusion path k connecting bubbles i and j and make the first-order approximation $\partial P_g/\partial x = \Delta P_{g,ij}/l_{ij,k}$. Here $\Delta P_{g,ij} = P_{g,i} - P_{g,j}$ is the bubble pressure difference, and $l_{ij,k}$ is the effective distance between bubbles i and j along diffusion path k in the liquid. Then we can write:

$$\frac{\partial V_{ij,k}}{\partial t} = -\frac{M_g \rho_l}{M_l \rho_g}\frac{D}{K^{px}} A_{ij,k}\frac{\Delta P_{g,ij}}{l_{ij,k}} \tag{7}$$

where for a diffusion path k, $\partial V_{ij,k}/\partial t$ is the volume change per time of bubble i caused by the mass transfer from bubble j, and $A_{ij,k}$ is the effective cross-sectional area through which this mass transfer occurs. We can also express the volume by $V_{ij,k} = Z V_m n_{ij,k}$, where $n_{ij,k}$ is the number of moles of gas added to (or lost from) bubble i via diffusion path k, V_m is the gas molar volume, and Z is gas compressibility factor. Thus,

$$\frac{\partial V_{ij,k}}{\partial t} = Z V_m \frac{\partial n_{ij,k}}{\partial t}, \tag{8}$$

where Z is treated as a constant that is calculated from PR EoS using a constant reservoir pressure and temperature. This is a reasonable assumption as bubble pressure variation has negligible impact on Z (Singh et al., 2022). For an isothermal mass transfer process, $\partial\mu/\partial P_g = V_m$ (Castellan, 1983). We approximate this differential as:

$$\Delta P_{g,ij} = \frac{\Delta\mu_{ij}}{V_m}. \tag{9}$$

From Eqs. (6)–(9), we recover Eq. (3) as

$$\frac{\partial n_{ij,k}}{\partial t} = -J_{ij,k} A_{ij,k} \Delta\mu_{ij} = -J_{ij,k} A_{ij,k} \times RT \times \left(\ln \frac{f_i}{f_j} \right), \tag{10}$$

where

$$J_{ij,k} = \frac{M_g \rho_l}{Z V_m^2 M_l \rho_g} \times \frac{D}{K^{px}} \times \frac{1}{l_{ij,k}}. \tag{11}$$

In the model, we simplify calculations of the cross-sectional area for mass transfer, $A_{ij,k}$, and the effective diffusion distance, $l_{ij,k}$. Unless stated otherwise, we will assume $A_{ij,k} = \min(A_{il,k}, A_{jl,k})$, where $A_{il,k}$ and $A_{jl,k}$ are the areas of the relevant gas/liquid interfaces of bubbles i and j, respectively, for diffusion path k. If we assume bubble i has N_i neighbor bubbles, where each neighbor bubble j has N_j diffusion paths to bubble i, then the total mass transfer rate for bubble i in BB method is given by:

$$\frac{\partial n_i}{\partial t} = \sum_{j=1}^{N_i} \sum_{k=1}^{N_j} \frac{\partial n_{ij,k}}{\partial t} = -(RT) \times \sum_{j=1}^{N_i} \sum_{k=1}^{N_j} (J_{ij,k} A_{ij,k}) \times \left(\ln \frac{f_i}{f_j} \right) . \tag{12}$$

We also typically assume the average mass transfer distance $l_{ij,k}$ is constant and equal to a characteristic pore throat length for the considered porous medium, i.e., $l_{ij,k} = \bar{l}$. This is consistent with previously developed theories (Xu et al., 2017) that have captured the ripening evolution in micromodel experiments using an average mass transfer length, even though the distances between the bubbles in the experiments vary. However, in this work, we will also explore the impact of replacing the constant mass transfer distance with variable mass transfer distances $l_{ij,k}$ using centroid-to-centroid distances between bubbles.

2.2. Analogy to ghost bubble method

In the GB method (Singh et al., 2022), an imaginary ghost bubble represents the liquid in its interaction with the gas bubbles (see Fig. 1). From a physical perspective, the purpose of a ghost bubble is to provide a relative measure of net mass transfer through a liquid phase or interface. It is defined such that it represents the stable state for the neighborhood bubble cluster at a particular time step. The ghost bubble is represented by the number of moles n_0, the chemical potential μ_0, and the fugacity f_0. Here, $f_0 \& \mu_0$ represent the equilibrium state for the gas bubbles in contact with the same liquid region. The ghost bubble fugacity for real gases is given as (Singh et al., 2022):

$$f_{0,l} = \prod_{i=1}^{N_l^{GB}} \left(f_i^{\frac{A_{i,l}}{\sum A_{i,l}}} \right)_{t'} , \tag{13}$$

where, at time t', the liquid region l is surrounded by N_l^{GB} gas bubbles, and $A_{i,l}$ is the interface area of gas bubble i with the liquid region l.

The mass interaction of a bubble i through liquid l can be expressed by modifying Eq. (2) for interaction between a gas bubble and ghost bubble:

$$\frac{\partial n_{i,l}}{\partial t} = -J'_{i,l} A_{i,l} (\mu_i - \mu_{0,l}) , \tag{14}$$

where $n_{i,l}$ is the number of moles transferred between bubble i and liquid region l, and $J'_{i,l}$ is the effective phase permeability to mass transfer in the GB method.

If we assume bubble i is adjacent to N_i^{GB} liquid regions, then Eq. (12) can be rewritten for the GB method as:

$$\frac{\partial n_i}{\partial t} = \sum_{l=1}^{N_i^{GB}} \frac{\partial n_{i,l}}{\partial t} = -(RT) \times \sum_{l=1}^{N_i^{GB}} (J'_{i,l} A_{i,l}) \times \left(\ln \frac{f_i}{f_{0,l}} \right) . \tag{15}$$

To derive a relationship between the phase permeabilities in the GB method and BB method, we consider a bubble i and its proportion of bubble neighbors N_i^* connected with the same liquid region l. For this case, Eqs. (12) and (14) yields

$$\frac{\partial n_{i,l}}{\partial t} = -J'_{i,l} A_{i,l} (\mu_i - \mu_{0,l}) = -\sum_{j=1}^{N_i^*} \sum_{k=1}^{N_j} J_{ij,k} A_{ij,k} \Delta\mu_{ij}. \tag{16}$$

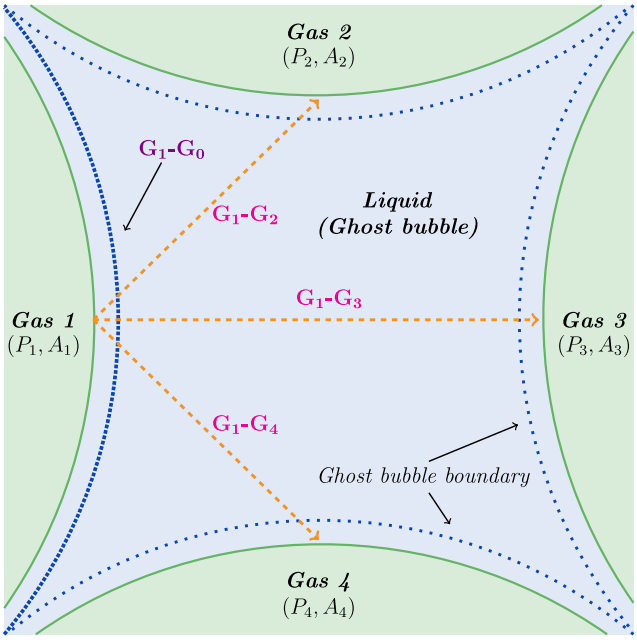

Fig. 1. Liquid region surrounded by four gas bubbles. The boundary of the ghost bubble region, shown by the *blue* dotted lines, coincides with the gas/liquid interfaces. They are shown here separately for clear demarcation. The mass transfer path (or area) for the gas bubble G_1 with ghost bubble region G_0 in the GB method is shown as $G_1 - G_0$. Mass transfer paths (in *orange*) for the same bubble G_1 with different bubbles in the BB method are shown as $G_1 - G_2$, $G_1 - G_3$, and $G_1 - G_4$.

The expression to the right accounts for the possibility of different numbers of diffusion paths N_j between bubble i and any of its neighbor bubbles j. From Eq. (16), we obtain a phase permeability expression for the interaction between bubble i and liquid region l in the GB method:

$$J'_{i,l} = \frac{\sum_{j=1}^{N_i^*} \sum_{k=1}^{N_j} J_{ij,k} A_{ij,k} \Delta\mu_{ij}}{A_{i,l} (\mu_i - \mu_{0,l})}. \tag{17}$$

In some cases with homogeneous bubble populations and pore geometries, we may approximate the areas for mass transfer ($A_{i,l}$ and $A_{ij,k}$) by the same constant value in both methods. As mentioned previously, we also set the effective diffusion path distances equal to a constant, $l_{ij,k} = \bar{l}$. Then $J_{ij,k} = J$ is also a constant and Eq. (17) reduces to

$$J'_{i,l} = \frac{J \sum_{j=1}^{N_i^*} N_j \Delta\mu_{ij}}{\mu_i - \mu_{0,l}}. \tag{18}$$

2.3. Level set method

Both the BB method and the GB method have been combined with the level set (LS) method for modeling the ripening as a series of quasi-static states. Previously, we explored the ripening of gas bubbles in the presence of a disconnected liquid by coupling the GB method with the multiphase level set (MLS) method and applying local volume conservation to both gas and liquid (Singh et al., 2022). For this purpose, the MLS method is a convenient tool as its phase-by-phase description, which uses one LS function per phase, facilitates simulations with volume conservation of more than one fluid phase (Helland et al., 2019; Jettestuen et al., 2021). In this work, we investigate the ripening of bubble populations surrounded by a continuous liquid with constant pressure P_l, which requires volume conservation of only the gas phase. For this purpose, we use the LS method, which is more efficient as it uses only one LS function to describe the gas/liquid interfaces (Jettestuen et al., 2021, 2013). On the other hand, simulations of

bubble ripening in three-phase systems will require the MLS method, as recently explored by Singh et al. (2023b).

Here we briefly describe the LS method (Jettestuen et al., 2021, 2013). The method uses a static LS function to describe pore space ($\psi > 0$) and solid phase ($\psi < 0$), while another LS function describes the gas phase ($\phi < 0$) and water phase ($\phi > 0$). These LS functions represent the signed distance to the interfaces, where $\psi = 0$ describes the pore/solid interfaces and $\phi = 0$ describes the gas/water interfaces. The level set equation for evolution of ϕ is given by (Jettestuen et al., 2013):

$$\frac{\partial \phi}{\partial \tau} + H(\psi)\left(P_c - \sigma\kappa\right)|\nabla\phi| + \frac{H(-\psi)}{\Delta x} S(\psi)\sigma\left(\nabla\phi \cdot \nabla\psi - \cos\zeta|\nabla\phi||\nabla\psi|\right) = 0 \ . \tag{19}$$

Here τ is a fictitious iteration time, H is the sharp Heaviside step function which separates the velocity terms for capillary-controlled motion in the pore space and the formation of contact angle on the pore walls, P_c is the gas bubble capillary pressure, σ is the gas-liquid interfacial tension, $\kappa = \nabla \cdot (\nabla\phi/|\nabla\phi|)$ is a scalar curvature field that represents the interface curvature at $\phi = 0$, S is a sign function, and Δx is the grid spacing. Further, ζ is a solid/fluid intersection angle measured through the gas between the gas/liquid interface and the solid surface. It is related to the contact angle θ (measured through liquid) by $\zeta = 180° - \theta$ and defined in terms of the unit normal vectors of the LS functions at equilibrium by

$$\cos\zeta = \frac{\nabla\phi}{|\nabla\phi|} \cdot \frac{\nabla\psi}{|\nabla\psi|}. \tag{20}$$

We make Eq. (19) non-dimensional by normalizing the actual values with a set of characteristic values for length l^*, interfacial tension σ^*, and capillary pressure $P_c^* = \sigma^*/l^*$, for the physical problem at hand (Jettestuen et al., 2021).

At equilibrium, the evolution of ϕ with Eq. (19) has reached a stationary state ($\partial\phi/\partial\tau = 0$) in which ϕ satisfies Eq. (20) for the contact angle, while the interface curvature in the pore space satisfies $\kappa = \kappa_0$, where κ_0 is given by the Young–Laplace equation:

$$P_c = P_g - P_l = \sigma\left(\frac{1}{r_1} + \frac{1}{r_2}\right) = \sigma\kappa_0 \ . \tag{21}$$

Here, P_g and P_l are the gas and liquid pressures, and r_1 and r_2 are the principal radii of curvature.

The gas volume and gas/liquid interface area are:

$$V = \int_\Omega H_\epsilon(\psi) H_\epsilon(-\phi) dV, \tag{22}$$

and,

$$A = \int_\Omega H_\epsilon(\psi)\delta_\epsilon(\phi)|\nabla\phi| dV, \tag{23}$$

respectively. Here, H_ϵ is a smoothed Heaviside function, δ_ϵ is a smoothed delta function, and $\epsilon = 1.5 \times \Delta x$ is the smoothening parameter.

While conserving a phase, we divide the area covered by it into continuous and isolated regions such that the volume of isolated regions is conserved while the volume of the continuous region are allowed to change. A continuous region is typically in contact with an open boundary. We create extended regions for each isolated region such that these extended regions cover the complete computational grid. The extended regions are used to redistribute the original/initial volume of the isolated regions during merging and splitting such that the total conserved volume of the phase is maintained until isolated regions interact with continuous domains. Refer to Jettestuen et al. (2021) and Singh et al. (2023a) for details on local volume conservation.

The capillary pressure of a gas bubble i at iteration time τ, subjected to local volume conservation, is calculated as (Saye and Sethian, 2011):

$$P_{c,i}(\tau) = \frac{V_i^{(0)} - V_i^{(\tau)}}{A_i^{(\tau)} \Delta\tau} \ . \tag{24}$$

Here, $V_i^{(0)}$ is the initial/original gas ganglion volume, while $V_i^{(\tau)}$ and $A_i^{(\tau)}$ are the ganglion volume and surface area at iteration time step τ, calculated using Eqs. (22) and (23), respectively, with integration over the domain corresponding to ganglion i. We link the resulting bubble capillary pressures to the computational grid which provides in effect a spatially and temporally varying scalar field for P_c used in the evolution Eq. (19) (Jettestuen et al., 2021).

Iterations with the LS Eq. (19) will lead to a deviation of ϕ from its signed distance nature. Hence, we reinitialize this LS function to its signed distance function at periodic intervals, following standard methods (Jettestuen et al., 2013; Osher and Fedkiw, 2003). The level set evolution converges to a steady state when the difference of ϕ between two reinitializations, denoted by m and n, in a small band (defined by b) around the zero contours of the level set function in pore space is less than a specified tolerance value:

$$\frac{\sum_\Omega H_\epsilon(\psi+\epsilon) H_\epsilon(\phi^n + \lambda) H_\epsilon(-\phi^n + \lambda)|\phi^n - \phi^m|}{\sum_\Omega H_\epsilon(\psi+\epsilon) H_\epsilon(\phi^n + \lambda) H_\epsilon(-\phi^n + \lambda)} < c\Delta x \ . \tag{25}$$

Here $\lambda = b \times \epsilon$ is the width of the convergence band. In this work, we use $b = 5$, $c = 0.001$, and a reinitialization interval of 10 iterations.

In the LS method, we approximate normal and advective velocity terms using a weighted essentially non-oscillatory (WENO) scheme with appropriate upwinding techniques, and the area and curvature terms with central differences. The iteration-time discretization uses a third-order Runge–Kutta method with a time step determined from a standard Courant–Friedrichs–Lewy (CFL) condition (Osher and Fedkiw, 2003). The LS methods are implemented within the SAMRAI framework (Hornung and Kohn, 2002; Hornung et al., 2006; Anderson et al., 2013) to enable parallel multiphase simulations with adaptive mesh refinement (AMR) using patch-based data structures (Helland et al., 2019; Friis et al., 2019). Recently, the LS methods with local volume conservation (Jettestuen et al., 2021) were also extended to provide AMR capabilities (Singh et al., 2023a). The current work uses this latter AMR capability for local volume conservation to assess grid resolution effects in simulations of ripening.

2.4. Combined method

In the combined method for ripening, an iteration step consists of simulating the interface motion to a stationary state using the LS method, followed by a mass transfer between the gas bubbles using either the GB or BB method (refer Singh et al. (2022) for a detailed workflow). The physical time in the ripening evolution is determined solely from the mass transfer step (assumption (i)). In the LS method, we initialize the system by calculating the signed distance function ϕ from a given fluid configuration. Then, we calculate a stationary state by iteratively solving Eq. (19). At each reinitialization step, we check for convergence using Eq. (25). In every LS iteration, we calculate the volume V_i, surface area A_i, and capillary pressures $P_{c,i}$, for each gas bubble i and use them to propagate the level sets to the stationary state. The mass transfer method takes as input V_i, A_i, as well as the gas bubble pressures $P_{g,i} = P_{c,i} + P_l$ from the stationary state.

Once the stationary state is reached, we identify different diffusive mass transfer paths for the BB method or, alternatively, different ghost bubble regions for the GB method. In the case of real gases, we calculate the fugacity of gas bubbles using PR EoS. In the GB method, we also calculate the fugacity of the ghost bubble. Then, we calculate the mass loss (or gain) Δn_i for a gas bubble i in a particular time step Δt by converting Eq. (12) (for BB method), or Eq. (15) (for GB method) to a finite difference equation. As an example, for Eq. (12) we can write:

$$\Delta n_i = -\Delta t \times (RT) \times \sum_{j=1}^{N_i} \sum_{k=1}^{N_j} (J_{ij,k} A_{ij,k}) \times \left(\ln \frac{f_i}{f_j}\right) \ . \tag{26}$$

Here, we control the physical time step Δt by setting a threshold for the maximum gas bubble volume change (for bubbles losing mass) V_{th}/t_{cf} and fixing the minimum bubble volume V_{floor} that is tracked

in the simulation. The step control factor t_{cf} is set to one initially. Typically, we use $V_{floor} = 4(\Delta x)^2$ and $V_{th} = 4(\Delta x)^2$ in 2D simulations, and $V_{floor} = 32(\Delta x)^3$ and $V_{th} = 10(\Delta x)^3$ in 3D simulations. We explore the impact of using different V_{th} and V_{floor} in Section 6.2.2.

The mass transfer from (or to) each bubble is used to update the mass of each bubble before the next LS evolution. As the chemical potential of gas is pressure-dependent, we assume in the numerical scheme that the pressure is constant for small changes in volume. Hence, after the mass transfer, we update the original bubble volumes $V_i^{(0)}$ and use them in Eq. (24) in the next LS evolution towards a new stationary state. After each LS and mass transfer step, we check if a thermodynamic equilibrium is reached. That is, we declare convergence in the combined method when the maximum bubble-pressure difference in the system is within a threshold value (in non-dimensional form):

$$\max_i\{P_{g,i}(t)\} - \min_i\{P_{g,i}(t)\} < \varepsilon \ , \tag{27}$$

where ε is an error threshold. In this work, we use $\varepsilon = 0.1$ unless stated otherwise.

A noteworthy point is the handling of potential mass transfer cyclicity within the bubble population, which typically can arise in the late stages of the evolution close to equilibrium. Since our method works on arbitrary pore geometry, we cannot have an *a priori* method to control cyclic mass transfer. Instead, we continuously monitor the evolution for changes in mass transfer direction between two bubbles. Once we detect reversed mass transfer, we reduce the time step by increasing the control factor t_{cf} alternately by a factor of two and three in consecutive cyclic mass transfer steps. When the cyclicity has disappeared, we perform three additional time iterations with the reduced time step. If the cyclicity remains absent, we reset t_{cf} to one for the next time iteration. If the cyclicity reappears, we increase the control factor t_{cf} to reduce the time step further. Intuitively, the cyclic mass transfer is linked to V_{th}, and a very high threshold can significantly impact the cyclicity observed in the results. Using a larger ε in Eq. (27) can also prevent cyclicity, but at the cost of accuracy.

3. Model validation

In this section, we validate the BB and GB methods against analytical solutions. We carry out the validation similar to our three-phase prediction validation in Singh et al. (2023b). We use a 2D homogeneous medium (with size 315 × 515 grid cells and grid spacing $\Delta x = 2$ μm) containing circular solid grains with a diameter of 165 μm. The solid grains are aligned on a square regular grid such that the distance between the centers of adjacent solid grains is 200 μm (see Fig. 2). The volume of each pore is $V_p = 1.86 \times 10^{-8}$ m^2 (volume in 2D is area). In these pores, the largest radius a circular bubble takes before it starts interacting with the solid grains is 58.9 μm, which corresponds to the bubble volume $0.59V_p$ (that is, the area of the maximal inscribed circle). The pore throat length (82 μm) is calculated as the distance between the centers of two maximal inscribed circles in adjacent pores minus their circle radii. This is the smallest distance between the interfaces of two neighboring bubbles with the largest possible circular shape. We add eight bubbles with volumes in the range between 1.26×10^{-8} m^2 and 1.50×10^{-8} m^2 in every other pore (see Fig. 2). The initial LS evolution forms the contact angle accurately on the grain surfaces and generates the initial pressure of each bubble.

The gas phase is air, which is assumed to be an ideal gas ($Z = 1$). The environment pressure and temperature are 101,325 Pa and 298.15 K. Henry's volatility for air in water is $K^{px} = 7 \times 10^9$ Pa and the diffusion coefficient is $D = 2 \times 10^{-9}$ m^2 s^{-1} (Xu et al., 2017). The molar mass M, and density ρ, of air and water are $M_g = 29$ g mol^{-1}, $M_l = 18$ g mol^{-1}, $\rho_g = 1.2$ kg m^{-3}, and $\rho_l = 1000$ kg m^{-3}. The solid grains are considered water-wet with contact angle $\theta = 10°$. We use the distance along the medial axis of the pore space between the arcs of two maximal inscribed circles placed in the bubble positions as the constant mass transfer length $l_{ij,k} = \bar{l} = 282 \times 10^{-6}$ m in the simulations.

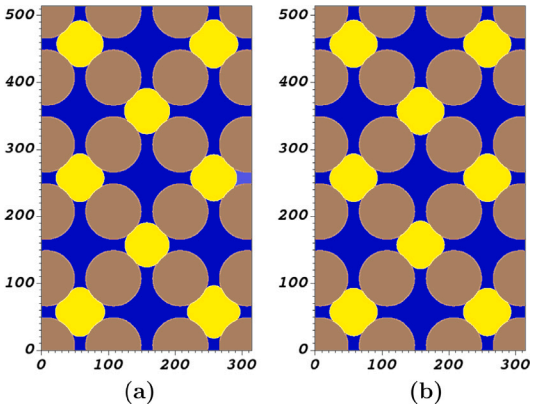

Fig. 2. Gas bubble configuration in water. (a) Initial, and (b) stable. Gas bubbles are in *yellow*, water is in *blue*, and solid grains are in *brown*.

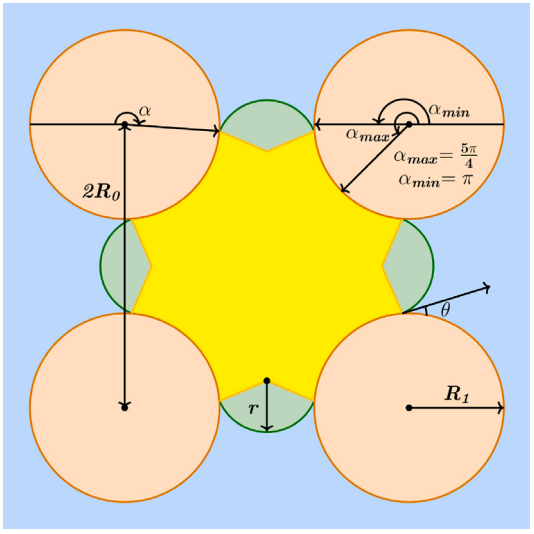

Fig. 3. Bubble geometry used in the calculation of analytical capillary pressure. The angle α determines the location of the gas/water/solid contact line. It can vary between π and $\frac{5\pi}{4}$. V_{body} is in *yellow*, V_{minor} is in *green*, water is in *blue*, and solid grains are in *brown*.

The characteristic parameters are set to $L^* = 2{\times}10^{-6}$ m and $\sigma^* = 10^{-4}$ N m^{-1}, which gives $P_c^* = 50$ Pa.

The analytic capillary pressures were calculated based on the equilibrium bubble volume in the simulations using equations determined by (Wang et al., 2021):

$$\begin{aligned} V_{total}(\alpha) &= 4V_{minor}(\alpha) + V_{body}(\alpha) \ , \\ V_{minor}(\alpha) &= \left(\frac{3\pi}{2} - \alpha - \theta\right) \frac{(R_0 + R_1\cos\alpha)^2}{\cos^2(\alpha+\theta)} \ , \\ V_{body}(\alpha) &= 4R_0^2 + (4\alpha - 5\pi)R_1^2 \\ &\quad + (2R_0 + R_1\cos\alpha)4R_1\sin\alpha \\ &\quad - 4(R_0 + R_1\cos\alpha)^2\tan(\alpha+\theta) \ . \end{aligned} \tag{28}$$

and,

$$r(\alpha) = -\frac{R_0 + R_1\cos\alpha}{\cos(\alpha+\theta)}. \tag{29}$$

Here, V_{total} is the total bubble volume, V_{body} is the body volume of the bubble in the center, and V_{minor} is the volume of the bubble protrusion in each pore throat (see Fig. 3). The angle α measures the area of grain surface covered by gas, while θ is the gas-water contact angle. $2R_0$ is the center-to-center distance between the grains, and R_1 is the radius

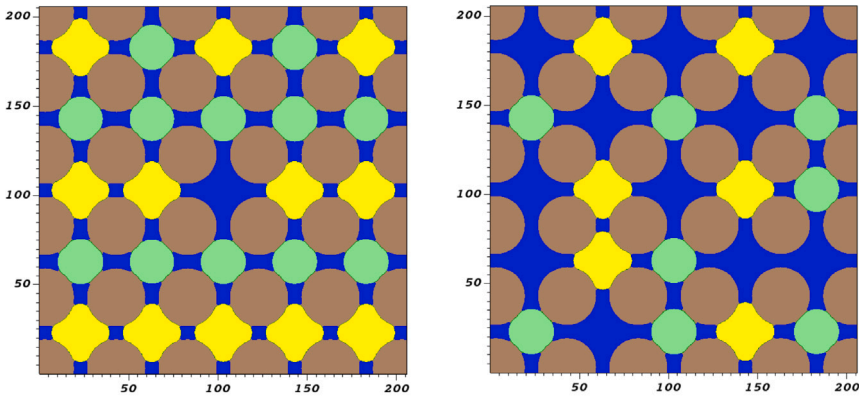

Fig. 4. Initial bubble distribution in the 2D homogeneous geometry (solid grains in *brown*) with 25 pores for (a) simulation 1 (and 5), and (b) simulation 2. In the initial distribution, larger bubbles are in *yellow*, and smaller bubbles are in *green*. The initial bubble distribution in simulation 5 is similar to that of simulation 1 shown in (a), except for small differences in bubble sizes that create slightly different average bubble sizes and gas saturation (see Table 3). The supporting information (Text S2 and Figure S1) describes initial bubble distributions for simulations 3 and 4.

of the solid grains. For details, refer to the supplementary information of Wang et al. (2021).

We carry out three simulations for BB and GB methods at different interfacial tensions corresponding to those used by Xu et al. (2017) in their experimental investigations. Tables 1 and 2 show the simulated and expected values for mass and capillary pressure for these simulations. The initial gas capillary pressure range for the bubble distribution is 771.2 Pa, 381.3 Pa, and 276 Pa for the interfacial tensions 71×10^{-3} N m^{-1}, 35.1×10^{-3} N m^{-1}, and 25.4×10^{-3} N m^{-1}, respectively. The value of α at equilibrium is determined to be 210.9° using the simulated equilibrium bubble volume in Eq. (28). This α is used in Eq. (29) to calculate the expected air–water capillary pressure. There is a 0.17% difference in the equilibrium volume predicted by the BB and GB methods. Since the level-set method conserves local volume, the initial total mass of the system decreases with decreasing interfacial tension (i.e., initial capillary pressure) at a constant environment pressure. The results highlight that there is negligible mass loss during ripening evolution in both methods. Mass conservation combined with reasonable capillary pressure at the stable state validates the thermodynamic equilibrium predicted by both models.

4. Comparison of bubble-to-bubble method and ghost bubble method

In this section, we compare the results from the GB and BB methods and analyze their computational performance. We use a 2D homogeneous porous medium (with size 206 × 206 grid cells and grid spacing $\Delta x = 5$ μm) formed by identical, circular solid grains aligned on a regular network (see Fig. 4). The geometry is similar to the one used in the previous section, except that it consists of 25 pores. The gas phase is distributed on this geometry as circles with radii taken from two different distributions generated using the *truncnorm* function in *Python* programming language. One of the distributions provides larger bubble radii than the other. All generated bubble radii are in the interval between 58.9 and 81 μm. As these bubbles will overlap with the solid grains, the corresponding bubble volume interval is between $0.59V_p$ and $0.84V_p$. The initial LS evolution uses this overlap to calculate a stationary fluid configuration that forms the contact angle accurately on the grain surfaces. The gas and water properties are the same as in the previous section. We use a constant mass transfer length $l_{ij,k} = \bar{l}$ in the simulations. The characteristic parameters are set to $L^* = 5 \times 10^{-6}$ m and $\sigma^* = 10^{-4}$ N m^{-1}, which gives $P_c^* = 20$ Pa.

We perform simulations with five different bubble distributions. In three of these distributions, nearly all the liquid regions have only two bubbles surrounding them (see Fig. 4(a)). For these dense bubble populations (simulations 1, 3, and 5), we use the pore throat length as mass transfer distance, $\bar{l} = 82$ μm. In the other two distributions, the liquid region is generally surrounded by more than two gas bubbles (see Fig. 4(b)). These cases (simulations 2 and 4) use a larger effective

Table 1
Comparison of BB method predictions against the expected values for mass and capillary pressure. The expected capillary pressure [Pa] is analytically calculated for the average equilibrium volume [1.36×10^{-8} m^2] at the predicted thermodynamic equilibrium. The total mass [$\times 10^{-7}$ kg] of bubbles at the initial converged state is used as a reference for the expected value at the end of the simulation. The pressure range at equilibrium is given in Pa.

Property	Expected	Simulated	Error (%)
IFT = 71×10^{-3} [N m^{-1}]			
Total mass	1.31	1.31	0.02
Capillary pressure	1836.97	1731.06	5.76
Pressure range	–	1.62	–
IFT = 35.1×10^{-3} [N m^{-1}]			
Total mass	1.30	1.30	0.01
Capillary pressure	908.07	855.71	5.77
Pressure range	–	4	–
IFT = 25.4×10^{-3} [N m^{-1}]			
Total mass	1.29	1.29	0.01
Capillary pressure	657.10	619.23	5.76
Pressure range	–	3.58	–

Table 2
Comparison of GB method predictions against the expected values for mass and capillary pressure. The expected capillary pressure [Pa] is analytically calculated for the average equilibrium volume [1.36×10^{-8} m^2] at the predicted thermodynamic equilibrium. The total mass [$\times 10^{-7}$ kg] of bubbles at the initial converged state is used as a reference for the expected value at the end of the simulation. The pressure range at equilibrium is given in Pa.

Property	Expected	Simulated	Error (%)
IFT = 71×10^{-3} [N m^{-1}]			
Total mass	1.31	1.31	0.15
Capillary Pressure	1844.28	1738.29	5.75
Pressure range	–	2.82	–
IFT = 35.1×10^{-3} [N m^{-1}]			
Total mass	1.30	1.30	0.01
Capillary Pressure	911.67	859.29	5.75
Pressure range	–	3.87	–
IFT = 25.4×10^{-3} [N m^{-1}]			
Total mass	1.29	1.30	0.16
Capillary Pressure	659.71	621.81	5.75
Pressure range	–	2.83	–

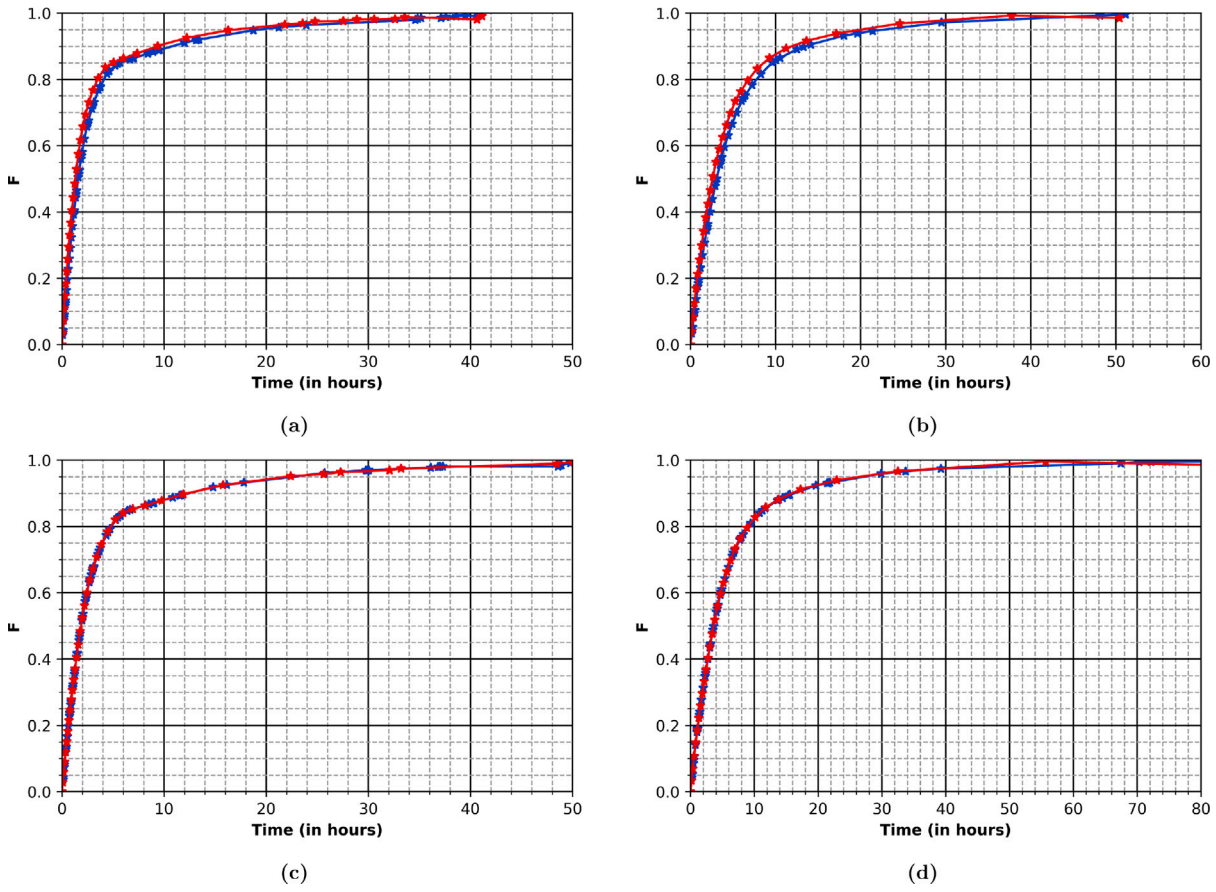

Fig. 5. Comparison of bubble distribution evolution towards equilibrium using BB method (in *blue*) and GB method (in *red*) with variable mass transfer area in (a) simulation 1 and (b) simulation 2, and with constant mass transfer area in (c)simulation 1 and (d) simulation 2. Here, F indicates the closeness to equilibrium, with $F = 0$ representing the initial condition and $F = 1$ representing the equilibrium condition.

Table 3
The interfacial tension σ [$\times 10^{-3}$ N m^{-1}], the number of bubbles in the pore space N_b, initial bubble volume deviation U_0 and average bubble volume V_{av} normalized by pore volume V_p, and gas saturation S_g for simulations comparing BB and GB methods.
Source: The interfacial tension values are adopted from Xu et al. (2017).

Simulation	σ	N_b	U_0/V_p	V_{av}/V_p	S_g
1	35.1	24	1.119	0.743	0.69
2	25.4	14	0.651	0.737	0.40
3	35.1	22	0.730	0.689	0.59
4	25.4	14	0.684	0.712	0.39
5	71.0	24	0.982	0.750	0.71

mass transfer length to account for bubbles separated by a vacant pore, $\bar{l} = 282$ μm. Hence, the five cases capture different sizes of ghost bubble regions. In the simulations, the GB method assumes simplified treatment of the mass transfer areas so that the phase permeability can be approximated by Eq. (18), while the BB method allows different mass transfer areas for each diffusion path in Eq. (12) using the phase permeability from Eq. (11).

We use a statistical indicator, the half of the total volume deviation U, to characterize the bubble distribution over time (Xu et al., 2017):

$$U = \frac{1}{2}\sum |V_i - V_{av}| \,, \tag{30}$$

where V_i is the volume of a single bubble, V_{av} is the average volume of the bubble distribution. This can be used to formulate an equilibrium indicator variable $F = 1 - \frac{U}{U_0}$, where U_0 is the initial deviation. F describes how close the bubble population is to the equilibrium, with equilibrium at $F = 1$. Table 3 shows the interfacial tensions and the properties of the bubble distributions used in the simulations.

Fig. 5(a) and (b) highlights the characteristic evolution nature of F (Xu et al., 2017), as obtained from simulations 1 and 2. The supporting information (Text S2 and Figure S2) presents similar results for simulations 3, 4, and 5. The evolutions calculated with the GB method and BB method are nearly coincident. The data points correspond to different times in the two methods since the physical time step is not fixed; instead, it is dynamically calculated during the simulation. The slight differences in the trendlines are likely caused by the simplifications made for determining the effective phase permeability of the GB method using Eq. (18), as the mass transfer areas used in the two methods are slightly different. We repeated the five simulations by assuming the mass transfer area in both methods is given by the minimum pore throat area (35 μm). Fig. 5(c) and (d) show the evolution of F for simulations 1 and 2, while the supporting information (Text S2 and Figure S2) provides similar results for simulations 3, 4, and 5 with constant mass transfer area. These graphs show that the constant area assumption makes the curves coincident for $F < 0.95$.

Despite the similarity in the bubble evolutions, computationally the two methods differ in speed and numerical mass-transfer cyclicity. During the simulations, we recorded the simulation time every 1000 LS iterations. Since the two methods run with dynamic time steps, we compare the values for the nearest F-values in Table 4. The GB method provides a speed-up of 1.7 to 2.2, which correlates closely with the ratio of LS iterations required to reach $F = 0.9$. At each quasi-static state in the simulation, one of the bubbles in the system has the highest mass loss rate. The maximum volume threshold V_{th} restricts the mass lost from this bubble at that particular state. The time step required for a fixed amount of mass loss is inversely proportional to the natural logarithm of the fugacity ratio (see Eq. (26)). In the GB method, the mass transfer occurs from a ghost bubble representing the

Table 4
Performance comparison of BB and GB method. Volume deviation F and total simulation time t [s] at the iteration (multiple of 1000) prior to LS iteration I_{GB} (for GB method) and I_{BB} (for BB method).

Simulation	GB method			BB method			Speed-up	$\frac{I_{BB}}{I_{GB}}$
	t	I_{GB}	F	t	I_{BB}	F		
1	850	53 270	0.901	1868	121 670	0.890	2.20	2.28
2	636	47 240	0.894	1216	93 470	0.898	1.91	1.98
3	634	43 220	0.927	1071	77 390	0.908	1.69	1.79
4	579	51 260	0.907	1034	91 460	0.903	1.79	1.78
5	804	49 250	0.917	1771	115 580	0.899	2.20	2.35

local equilibrium. Hence, its fugacity difference with the neighboring bubbles is smaller than the fugacity difference between bubble pairs in the BB method. This allows a larger time step for mass transfer in the GB method than the BB method (see Fig. 5). In our simulations, we observed that cyclicity near equilibrium was more prominent in the case of the GB method. For example, in Fig. 5(b), the GB method curve shows slight oscillation for $F > 0.95$. Ghost bubble fugacity impacts mass transfer for multiple bubbles. So, in the GB method, each instance of cyclicity also affects multiple bubbles.

The results show that the GB and BB methods are akin to each other. The GB method provides faster computation but is prone to cyclicity issues near equilibrium. Thus, it is more suitable in scenarios with fewer possibilities for cyclicity, like in idealized porous media with smooth pore geometry changes. On the other hand, the BB method is suitable in more complex scenarios where pore geometry changes sharply, and small changes in bubble volume can cause large pressure differences. As mentioned earlier, it is possible to control the impact of mass transfer cyclicity in the GB method by reducing V_{th}. Alternatively, one can improve the BB method's computational performance by increasing V_{th}.

5. Impact of pore geometry on ripening

It has been widely reported that pore geometry affects Ostwald ripening dynamics (de Chalendar et al., 2017; Xu et al., 2017, 2019; Singh et al., 2022; Yu et al., 2022). This section uses the BB method to investigate geometry effects on gas bubble ripening at the scale of a single pore throat connected by two pores, followed by investigations on a 3D representation of a typical homogeneous micromodel geometry with a fixed depth. We comment on important parameters that can affect the time scale of ripening.

5.1. Ripening in a 2D isolated pore pair connected by different pore throats

Previously, we have investigated different Ostwald ripening scenarios between two gas bubbles in an isolated pore pair connected by a converging/diverging pore throat Singh et al. (2022). The simulations confirmed earlier observations of de Chalendar et al. (2017) that in porous media mass transfer direction depends not only on the bubble volume but also on the pore geometry. However, a key point that still requires investigation is the impact of pore throat shape on the ripening dynamics. The previous investigations used a fixed pore throat geometry consisting of two truncated triangles (Singh et al., 2022). Here, we explore three different pore throats (geometry 1, 2, and 3), each formed by a section with different truncated triangles and a section with two parallel plates separated by 20 μm, see Fig. 6(a).

The three geometries (discretized with 350 × 140 grid cells and grid spacing 1 μm) consist of two circular pores (with radius 60 μm) connected by the different asymmetrical pore throats. The triangular section in the pore throats contains one truncated triangle with different slopes in geometry 1 and 2, while geometry 3 forms two truncated triangles with different slopes in this section, see Fig. 6(a). In all three geometries, we ensure that the initial pressure difference and distance between the bubble interfaces are the same in all three geometries. If

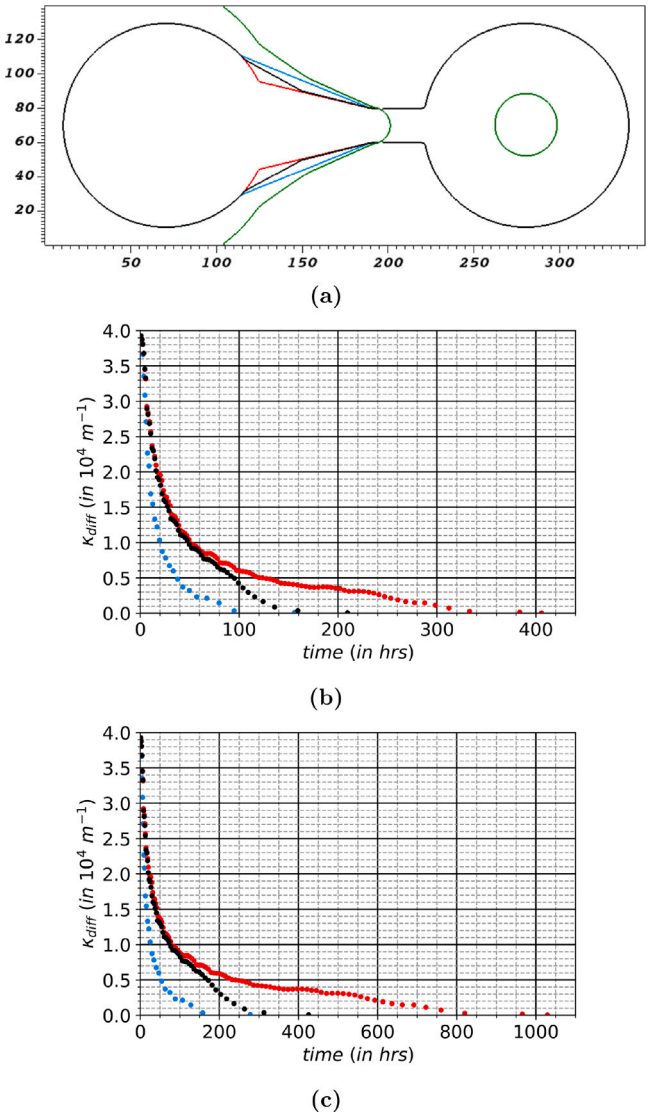

Fig. 6. Impact of pore throat geometry on ripening. (a) Different geometries, (b) curvature difference evolution curve with varying mass transfer area, and (c) curvature difference evolution curve with constant mass transfer area. Geometry 1 is in *blue*, geometry 2 in *red*, and geometry 3 in *black*. Figure (a) also shows the initial zero contours $\phi = 0$ (in *green*) representing the brine/CO_2 interfaces in the pore space. Note that $\phi = 0$ extends into the solid phase for accurate formation of the contact angle on the pore walls.

we use a constant mass transfer distance $\bar{l}$ in all cases, the mass transfer rate will solely depend on the change in interfacial area and capillary pressure of the bubbles as they grow or shrink in the pore space. Both these parameters are functions of the pore throat geometry. To ensure equal pressure difference initially in the three geometries, the interface of the left bubble lies in the parallel section of the pore throat, while the other bubble resides within the circular pore. The initial volume of the smaller bubble is 1.04×10^{-9} m^2. The pressure of the smaller bubble is lower than the larger bubble, so the bubble to the left loses mass during the ripening evolution. This corresponds to a situation where the interface radii of both bubbles increase with time (Singh et al., 2022).

We consider a fluid system with supercritical CO_2 as the non-wetting phase and brine as the wetting phase. The environment pressure and temperature are 15 MPa and 323.15 K. Henry's volatility for CO_2 in brine is $K^{px} = 8.46 \times 10^8$ Pa (Sander, 2015) and the diffusion coefficient is $D = 7.42 \times 10^{-9}$ m^2 s^{-1} (Cadogan et al., 2014). The CO_2-brine interfacial tension is $\sigma = 32.6 \times 10^{-3}$ N m^{-1} (de Chalendar et al.,

2017). The molar mass and density of CO_2 and brine are $M_g = 44$ g mol^{-1}, $\rho_g = 699.75$ kg m^{-3}, $M_l = 18$ g mol^{-1}, and $\rho_l = 994.43$ kg m^{-3}, respectively (Lemmon et al., 1997). We use a constant mass transfer length $\bar{l} = 200$ μm, and $\varepsilon = 0.05$. The solid grains are water-wet with a contact angle of $\theta = 10°$. The characteristic parameters are set to $L^* = 1 \times 10^{-6}$ m and $\sigma^* = 10^{-4}$ N m^{-1}, which gives $P_c^* = 100$ Pa.

Fig. 6(b) shows the evolution of curvature difference between the bubbles, given as $\kappa_{diff} = \Delta P_g/\sigma$. Since the bubble to the right only grows radially, the rate of change of κ_{diff} relates directly to pressure changes of that bubble. This rate of change depends strongly on the slope of the pore throat. A larger slope (cf. geometry 1) yields a faster ripening towards equilibrium because the increase of interfacial area and the decrease of capillary pressure that the left bubble experiences for a given reduction in bubble volume are more significant. The final volume of the circular bubbles is different in all the cases: 1.54×10^{-9} m^2 (geometry 1), 2.97×10^{-9} m^2 (geometry 2), and 2.16×10^{-9} m^2 (geometry 3). So, we can conclude that the volume of the smaller bubble and the time to reach equilibrium increases with decreasing pore throat slope. The different equilibrium volumes of the circular bubble also show that the equilibrium pressures also depend on the shape of the pore throat.

We repeat the simulations by assuming a constant mass transfer area equal to the width of the parallel pore throat region (20 μm). Then it is only the pressure–volume behavior that could lead to different ripening evolutions in the three geometries. Fig. 6(c) shows that the evolutions of κ_{diff} are similar to those in Fig. 6(b). However, since the constant mass transfer area is less than the minimum bubble interfacial area used in Fig. 6(b), the bubbles take a longer time to reach equilibrium this time. Initially, the ratio of mass transfer areas in the two sets of simulations is 1.3, but it increases to an interval ranging from 2.02 to 2.87 in the three geometries at equilibrium. Meanwhile, the ratio of equilibrium times for the same geometry in the two simulation sets ranges from 1.8 to 2.5. The impact of mass transfer area can be observed in Fig. 6(b) and (c). The curves are nearly proportional during initial evolution when the ratio of the two mass transfer areas is nearly constant, but then the evolutions start to deviate slightly as the ratio increases. Overall, the results show that the choice of mass transfer area in the model is important for the time scale of the ripening without significantly changing the nature of the evolution, whereas the pressure–volume behavior (which depends on pore geometry) impacts both the time scale and how the ripening evolves. This demonstrates the importance of using a suitable pore throat shape for the idealization of the pore geometry in studying Ostwald ripening (e.g., de Chalendar et al., 2017).

5.2. Ripening in 3D micromodel geometries

We extend the analysis from the last section to a porous medium containing multiple pores. For this purpose, we utilize the experimental investigations presented by Xu et al. (2017) which were later also studied by Mehmani and Xu (2022a) using a pore-network model (PNM). Xu et al. (2017) experimentally studied Ostwald ripening using air and surfactant solution in a homogeneous glass micromodel. In this micromodel, the 2D structure of pores and grains has the same specifications as the geometry used in Section 4. However, the micromodel has a depth that varies gradually from 26.4 ± 1 μm in the pores to 14.7 ± 1 μm in the pore throats to provide a 3D effect on the 2D array. Mehmani and Xu (2022a) compared PNM results with one of the experiments from Xu et al. (2017) using a 3D semi-cubic pore network containing a total of 120 (15×8) pores. The varying micromodel depth makes it difficult to create a precise replica of it. Therefore, we perform simulations with the BB method using a homogeneous pore geometry that is constant with depth and contains 120 pores (see Fig. 7(a)), for comparison against the PNM results (Mehmani and Xu, 2022a) and the experimental results (Xu et al., 2017). This geometry, with cylindrical solid grains, is sandwiched by solid plates at the top and bottom. The resulting 3D computational domain contains $430 \times 430 \times 15$ grid cells with a grid spacing $\Delta x = 5$ μm. The depth of the pore space and each of the solid plates is 25 μm.

Consistent with the published data (Xu et al., 2017; Mehmani and Xu, 2022a), we populate the pore space with 73 bubbles. The interface areas for the larger bubbles in the simplified geometry are typically 1.6 ($= 5/3$) times larger compared to the actual micromodel. The volume of each pore is $V_p = 4.65 \times 10^{-13}$ m^3 in our simulations. We use $V_{th} = 12(\Delta x)^3$ to limit the time step. We carry out two sets of simulations, one with a constant mass transfer length $l_{ij,k} = 282$ μm, and another with $l_{ij,k}$ approximated by the centroid-to-centroid distance between bubbles. The mass transfer area for a diffusion path between two bubbles is the smallest area of the two relevant interfaces of the bubbles. The gas-liquid interfacial tension is $\sigma = 25.4 \times 10^{-3}$ N m^{-1} and the contact angle is $\theta = 10°$. The environment pressure and temperature are 101,325 Pa and 293 K. The other simulation parameters are the same as in Section 4. Following Mehmani and Xu (2022a), we carry out ten simulations with slightly different bubble distributions and use the average value to remove spatial bias from the analysis.

Fig. 7(b) shows the non-linear relation between bubble capillary pressure (P_c) and bubble volume (V_b) for bubble growth in a single pore used in our simulation (*blue* dots). While the coupled model calculates such data directly during the ripening simulation, here we have generated this curve using the LS model alone on the simplified geometry by calculating capillary equilibrium states for a series of different bubble volumes (see Appendix A). On the other hand, the different pore geometries used in the PNM and the experiments allowed accurate linear approximations of the $P_c(V_b)$ curves for $V_b > V_{ci}$ (Xu et al., 2017; Mehmani and Xu, 2022a). Here, the critical volume of a bubble, V_{ci}, is the volume at which the bubble has the minimum pressure, which in a case with zero contact angle would correspond to a bubble (in a 2D section) shaped by the maximal inscribed circle in the pore. Further, m is the slope of a line that approximates the $P_c(V_b)$ function for bubble volumes $V_b > V_{ci}$ (that is, the range at which the bubble interacts with the grains) (Mehmani and Xu, 2022a). Fig. 7(b) shows the linear approximation from the micromodel experiment (*solid black*) as well as a linear fit to our simulated curve (*dashed orange*). From the simulated curve we obtain $V_{ci-BB} \approx 0.56 \times V_p$ and $m_{BB} \approx 1.73 \times 10^{17}$ m^{-4}. The values in the PNM and micromodel experiment were as follows: $V_{ci-PNM} \approx 0.52 \times V_p$ and $m_{PNM} \approx 3.0307 \times 10^{16}$ m^{-4}, and $V_{ci-Exp} \approx 0.6 \times V_p$ and $m_{Exp} \approx 1.6 \times 10^{17}$ m^{-4}, respectively (Mehmani and Xu, 2022a). The value of these two parameters, V_{ci} and m, depends on the gas-liquid contact angle and micromodel depth (see Appendix A for a detailed analysis). Obviously, the difference in the $P_c(V_b)$ curves between our simulations and the micromodel experiments is due to the uniform depth in the simplified geometry used in the simulations. Mehmani and Xu (2022a) attributed the different values of these two parameters to the semi-cubic nature of the PNM geometry and compensated for the difference by updating the depth of their geometry.

Fig. 7(c) shows the bubble-size distribution at different times in our ripening simulations for both the case with constant mass transfer length and the case with a centroid-to-centroid distance between the bubbles as mass transfer lengths. The wide initial distribution progressively coarsens such that the average bubble volume is between $0.7V_p$ and $0.9V_p$ after 80 h. The homogeneous medium with identical pores ensures that both the bubble volume distribution and bubble pressure distribution narrow over time. After 40 h, bubbles with initial volumes less than $0.45 \times V_p$ are typically lost from the system. The distribution's coarsening rate decreases with evolution. This decreasing rate results from the decreasing growth rate of bubbles with volume in the range between $0.7V_p$ and $0.8V_p$, and decreasing loss rate of bubbles with volume in the range between $0.8V_p$ and $0.9V_p$. Fig. 7(c) also shows that the simulations with constant and varying mass transfer lengths have similar evolutions, with the constant mass transfer length simulations demonstrating a marginally faster ripening rate.

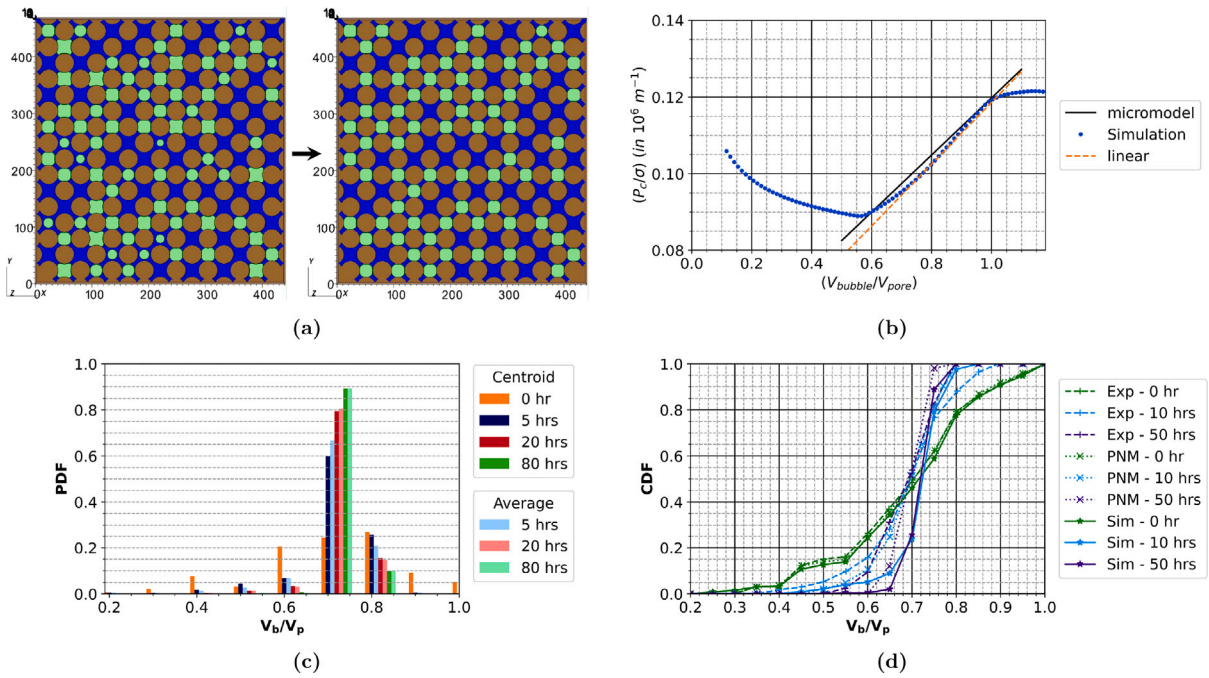

Fig. 7. Comparison of simulations with BB method against micromodel experiment and PNM simulation results. (a) Typical initial distribution with 73 bubbles (left), and equilibrium distribution (right), from BB simulation in 15 × 8 pore space (gas in *green*, liquid in *blue*, and solid grains in *brown*), (b) capillary pressure vs. volume curve for bubble growth in a single pore of depth 25 μm, (c) bubble-size distribution in our simulation at different times, and (d) comparison of cumulative bubble size distribution in our simulation with PNM (Mehmani and Xu, 2022a) and micromodel experiment (Xu et al., 2017). On the x-axis, the volume of bubbles is normalized by the volume of a single pore.

Differences in pore geometry lead to different rates of coarsening. Fig. 7(d) compares the cumulative bubble-size distribution of our simulation (for the case with a centroid-to-centroid distance between bubbles as mass transfer length), the PNM (Mehmani and Xu, 2022a), and the micromodel experiment (Xu et al., 2017). The comparison shows that our simulations predict a faster coarsening rate than the PNM simulations, which in turn predicts a faster rate than the micromodel experiments. The difference in ripening rates suggests that the different pore geometries impact the results through different mass transfer areas and $P_c(V_b)$ behavior (as investigated in Section 5.1).

Mehmani and Xu (2022a) calculated a consistent value for the mass transfer area based on an equivalence relation between mass transfer area, mass transfer length, and $P_c(V_b)$-function in the PNM and the micromodel. This resulted in a higher mass transfer area in the PNM (2.716×10^3 μm^2) than in the micromodel ($35 \times 14.7 = 5.145 \times 10^2$ μm^2). However, we calculate the gas-liquid interfacial area (including the effects of curvature) for each bubble corresponding to a uniform depth of 25 μm. This leads to a mass transfer area in our simulations that always will be much larger than $35 \times 25 = 8.75 \times 10^2$ μm^2. Compared to the micromodel experiment, our model predicts larger areas for the larger bubbles. This larger mass transfer area leads to a higher coarsening rate in our simulation.

Finally, the $P_c(V_b)$ curve in the PNM model, micromodel experiments, and our simulations differ in V_{ci} as well as slope m. Mehmani and Xu (2022a) incorporated an almost linear approximation of the $P_c(V_b)$-function. Still, their model predicts faster coarsening which is more distinct at 50 h. The authors hypothesize that the ripening rate is faster than in the experiments due to the use of an almost linear function with a positive slope to represent the flat region of the $P_c(V_b)$ function near V_{ci} (Mehmani and Xu, 2022a). Our simulations yield a non-linear $P_c(V_b)$-curve, with a flat region for $V_b > V_{ci}$ near V_{ci}, followed by an increasing slope and then a decreasing slope with higher V_b. Furthermore, in simulations, it is essential to use V_{ci} that conforms with the experiment. If V_{ci} deviates from the experimental value, the simulation will use a $P_c(V_b)$-curve with a slope of the opposite sign than that obtained in the experiment for the bubble volume interval between the experimental and modeled V_{ci}. This will impact the compliance of ripening rate and mass transfer direction between simulation and experiment. As discussed in Section 5.1, the slope of the $P_c(V_b)$ curve is strongly related to the pore-throat geometry, and it impacts the coarsening rate in that a higher slope leads to a larger change in bubble pressure for the same change in bubble volume. Despite the differences in pore geometry and ripening rate; our simulation, the PNM, and the micromodel experiment predict that the equilibrium bubble volume is around $0.7V_p$.

6. Impact of initial spatial bubble distribution on ripening

In Section 5.2, we used average values from multiple simulations to remove spatial bias from the results. In this section, we use the BB method to investigate the impact of spatial bubble distributions on the ripening evolution in 2D and 3D porous media.

6.1. 2D homogeneous porous medium

The ripening evolution of a bubble population depends on the spatial distribution of bubbles with different pressures (Mehmani and Xu, 2022a). Here, we perform simulations to investigate how different patterns with small and large bubbles in 2D homogeneous media (similar pore geometries as used in Section 4) create different ripening evolutions, as quantified by the equilibrium indicator F over time. An objective is to determine spatial bubble-size patterns that conform to the theoretical model for gas bubble ripening in homogeneous media proposed by Xu et al. (2017). This model assumes that the area and length for diffusive mass transfer are given by the minimum throat area and the pore throat length. A further assumption is that the number of bubbles in the system remains unchanged during the evolution. If l_0 is the average mass transfer distance, t is the time, and n_{av} is the average number of neighbors to a given bubble; then the theoretical model predicts that a plot of F on a time frame, $\tau = \sigma t n_{av}/l_0$, will collapse the curves for different evolutions on a single exponential curve given by $F = 1 - \exp(-\tau/b_{eq})$ (Xu et al., 2017). Here, b_{eq} is a fluid phase

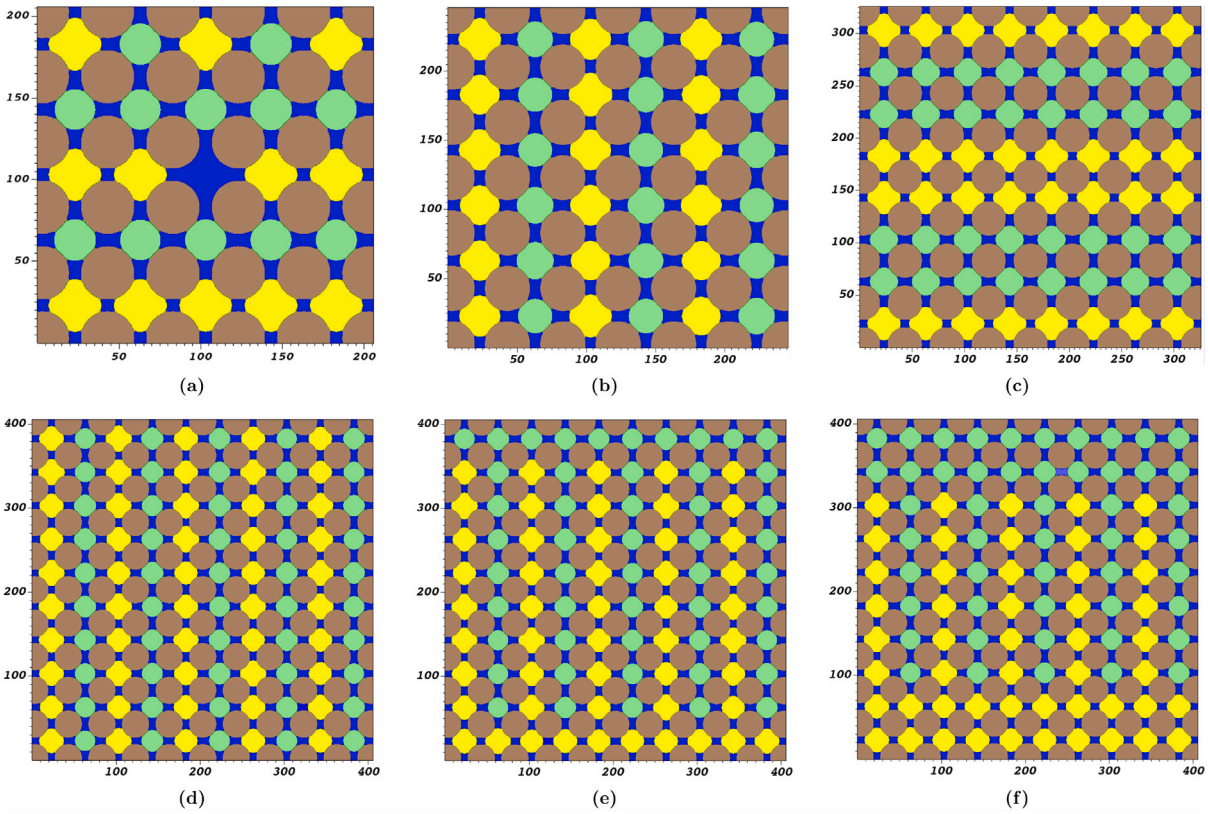

Fig. 8. Initial bubble distribution for different simulations: (a) simulation 1 (25 pores, 206 × 206 grid cells), (b) simulation 6 (36 pores, 246 × 246 grid cells), (c) simulation 7 (64 pores, 326 × 326 grid cells), (d) simulation 8 (100 pores, 406 × 406 grid cells), (e) simulation 8 modified with a pore layer of large bubbles at the bottom and small bubbles at the top, and (f) simulation 8 modified with two pore layers of large bubbles at the bottom and small bubbles at the top. In the distributions, larger bubbles are in *yellow*, and smaller bubbles are in *green*. The grid spacing is 5 μm.

and pore geometry based scaling factor, and n_{av} can be calculated as $n_{av} \approx (V_{pore}/V_{av})S_g n_0$, where S_g is the gas saturation, and n_0 is the average pore connectivity. In this section, we use $F-\tau$ plots to compare different spatial distributions.

The parameters used in the different simulations are given in Table 5. The other simulation parameters are the same as in Section 4. We carry out two sets of simulations, one set has 24 bubbles in a 25 pore system (simulations 1–5), and the other set (simulations 6–8) is a comparison of evolution with 36, 64, and 100 bubbles with one bubble in each pore. The initial bubble-size distributions of small and large bubbles in simulations 1–5 are different, resulting in slightly different average bubble sizes and gas saturation (see Table 5). For simulation 6 (36 pores), we select the set of small bubbles and large bubbles from the same normal distributions as in simulation 8 (100 pores) to investigate the effects of sample size on ripening. For simulation 7 (64 pores), we choose two fixed volumes for the large and small bubbles, 1.94×10^{-8} and 1.64×10^{-8} m^2 (volume in 2D is area). For simulation 8, we also make two additional modifications to the original bubble distribution and perform corresponding simulations while maintaining the specifications in Table 5. In the first case, we place large bubbles in the entire bottom layer of pores and small bubbles in the entire top layer, while in the second case, we place large bubbles in the two bottom layers of pores and small bubbles in the two top layers. Fig. 8 shows the initial bubble patterns used in the simulations.

Fig. 9(a) shows the different $F - \tau$ curves for the first set of simulations. Conforming to the theory, we observe that the values from different simulations collapse onto a single curve. We fit an exponential curve and obtain $b_{eq} = 1.303 \times 10^7$ Pa s. The common curve deviates from the strictly exponential curve for $F > 0.85$. We explore this behavior through the second set of simulations.

To confirm that the deviation is not a result of sample size, we compare simulation 6 (36 pores) and simulation 8 (100 pores). As shown in Fig. 8(b) and (d), the initial bubble patterns in these simulations are similar with alternating pore layers containing smaller and larger bubbles. Fig. 9(b) shows that the $F-\tau$ plots for these simulations follow the same trend line, suggesting that the deviation from the exponential curve does not depend on the sample size. The evolution follows the same trend for the same spatial distribution of bubbles with higher and lower pressure, irrespective of sample size.

In simulation 7 (64 pores), the initial, layered bubble pattern displays a scenario where every small bubble interacts with only one large neighbor bubble and vice versa, as shown in Fig. 8(c). Fig. 9(b) shows that the evolution in this case closely follows the exponential curve to equilibrium.

Fig. 8(d)–(f) shows the initial bubble patterns for simulation 8 (100 pores) and its two modified cases that contain one and two pore layers with large and small bubbles at the top and bottom of the sample. Obviously, the increased layering of small and large bubbles reduces the number of bubbles that have neighbor bubbles of the other size. As

Table 5
The number of pores N_p, interfacial tension σ [$\times 10^{-3}$ N m^{-1}], initial bubble volume deviation U_0 and average bubble volume V_{av} normalized by pore volume V_p, and gas saturation S_g for different simulations.

Simulation	N_p	σ	U_0/V_p	V_{av}/V_p	S_g
1	25	35.1	1.119	0.743	0.694
2	25	25.4	0.902	0.726	0.678
3	25	71.0	0.581	0.753	0.700
4	25	25.4	0.674	0.729	0.682
5	25	35.1	0.541	0.699	0.655
6	36	35.1	0.984	0.718	0.711
7	64	71.0	2.064	0.767	0.719
8	100	35.1	2.914	0.722	0.711

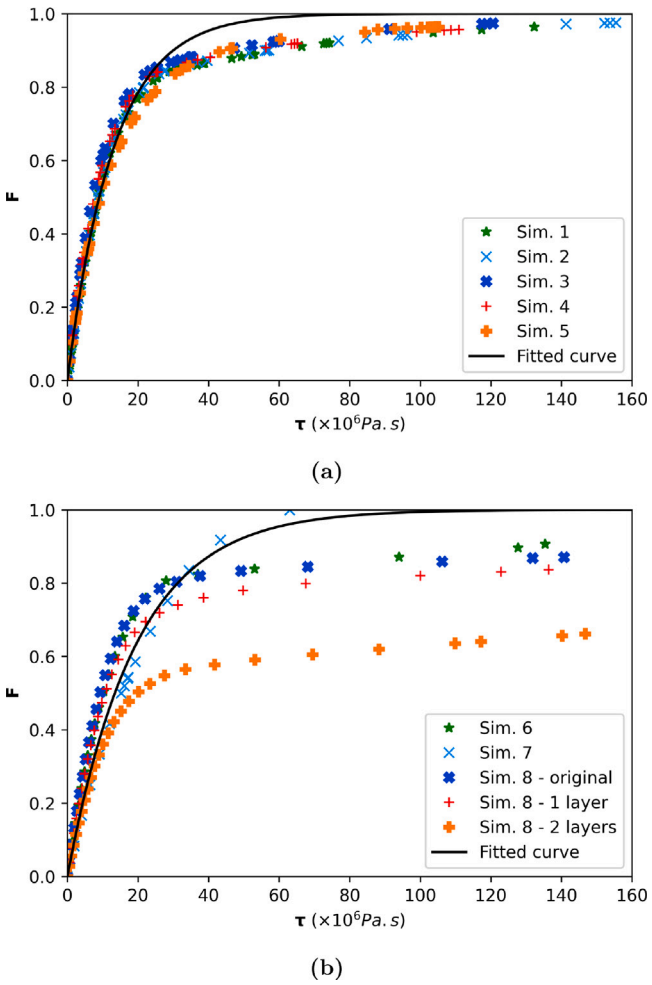

Fig. 9. Evolution of bubble distribution to equilibrium in the different simulations: (a) same spatial distribution and different size distributions in 25 pores (simulations 1–5), and (b) different spatial distributions (simulations 6–8). The figures also show fitted curves to the simulation results based on the theoretical model (Xu et al., 2017). Here, F indicates the closeness to equilibrium, with $F = 0$ representing the initial condition and $F = 1$ representing the equilibrium condition.

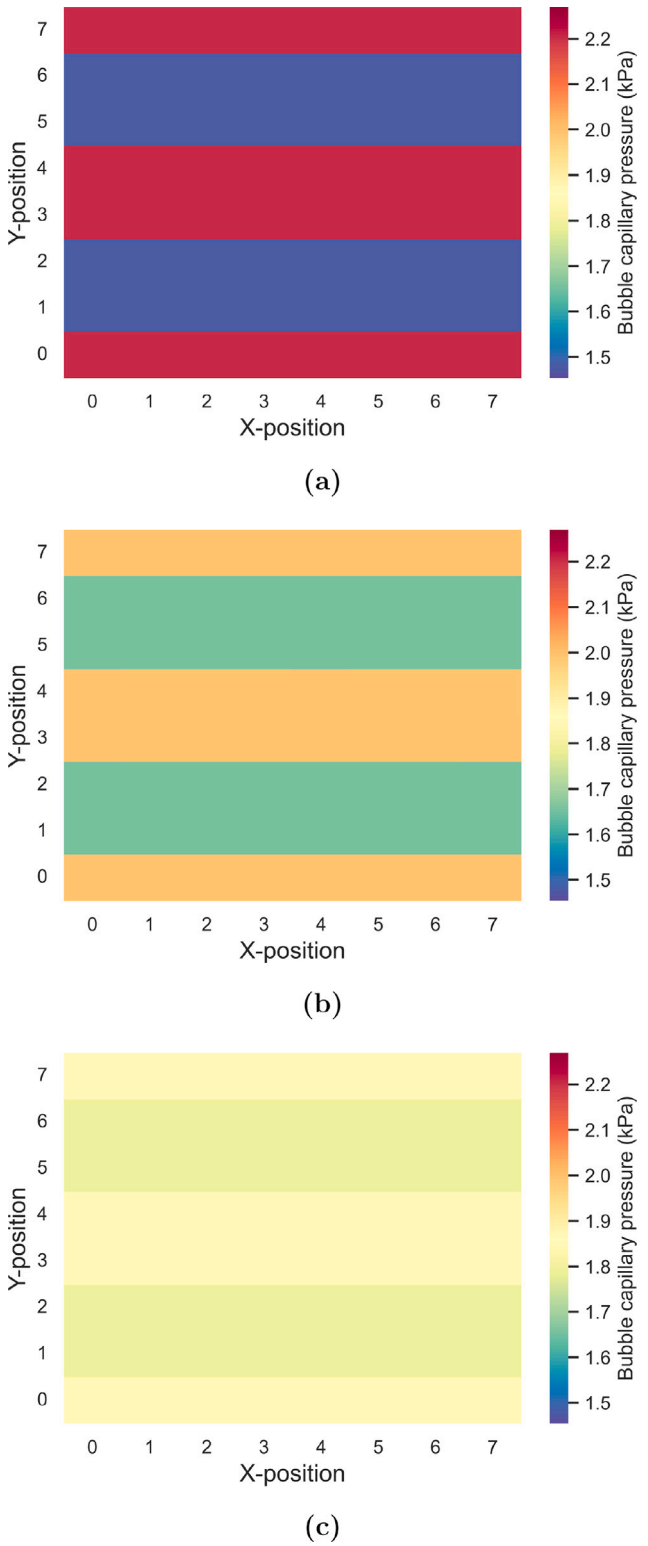

Fig. 10. Bubble capillary pressure evolution during Ostwald ripening in simulation 7 (local equilibrium). The equilibrium indicator, F (in %), for the different images are: (a) 8.3, (b) 58.6, and (c) 91.8.

shown in Fig. 9(b), this reduces the mass transfer rate and promotes an early deviation from the exponential curve.

The spatial location of bubbles with contrasting pressures can explain the deviation of the simulation results from the theoretical exponential curve. Figs. 10 and 11 show the bubble capillary pressure evolution during Ostwald ripening for simulation 7 (Fig. 8(c)) and simulation 8 with two modified bubble layers at top and bottom (Fig. 8(f)), respectively. Here, the pressure of a bubble is represented by a color on a square pore element. For simulation 7, the pressure change decreases uniformly in the entire pore geometry over time while the location of the pressure gradient remains unchanged. We refer to this type of ripening regime as a *local regime* where local equilibrium (e.g., equilibrium between bubble neighbors with different initial pressure) ensures global equilibrium in the distribution.

On the other hand, for simulation 8 with two modified bubble layers at the top and bottom, the location of the pressure gradient in the geometry changes as the evolution proceeds. As expected, it also leads to a situation where the bubbles with minimum and maximum pressure reside on the opposite sides of the geometry (Fig. 11). Such scenarios lead to slower mass transfer since the mass has to be transferred sequentially through many bubbles before the system reaches thermodynamic (or global) equilibrium. We refer to this type of ripening behavior as a *global regime*. The deviation from the exponential curve in Fig. 9 highlights the switch from a local ripening regime dominated mass transfer to a global ripening regime dominated mass transfer. Comparison of Figs. 10 and 11, and the corresponding $F - \tau$ plots in Fig. 9, suggests that ripening in the local regime towards

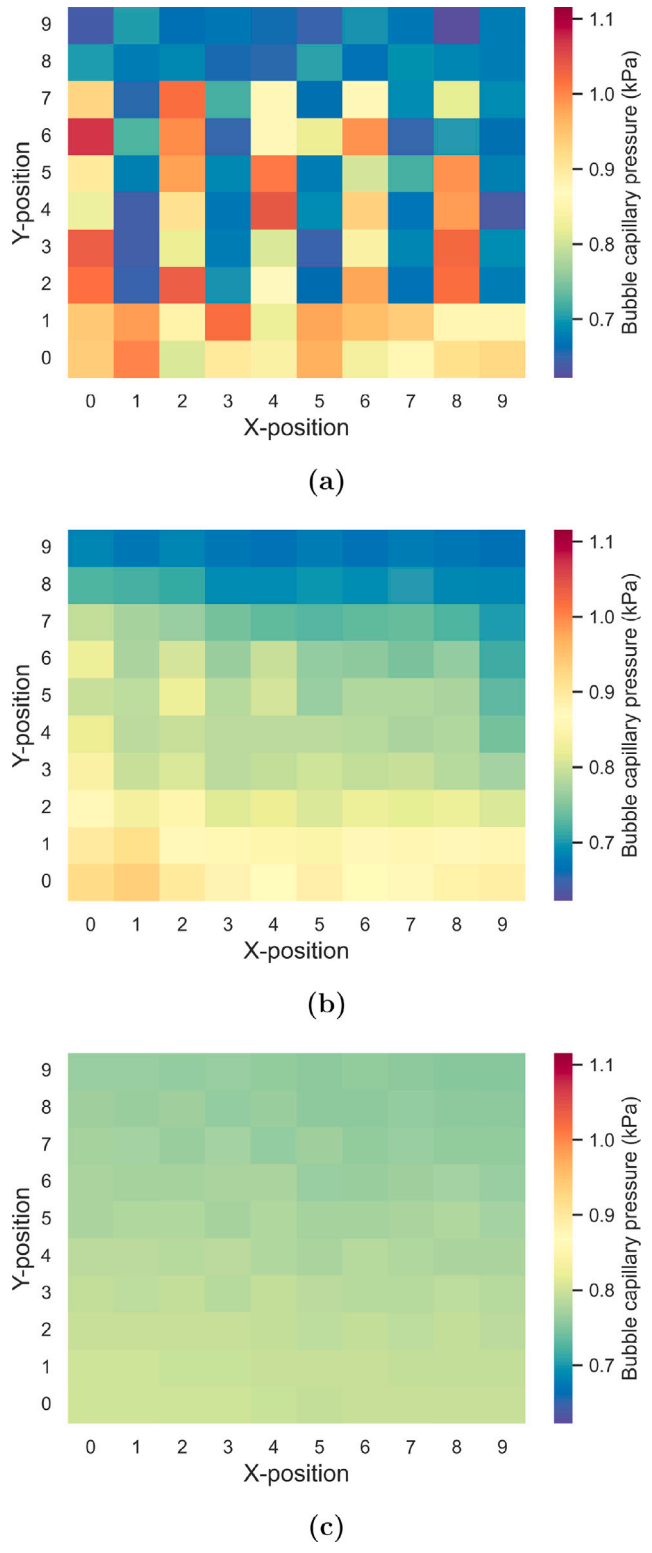

Fig. 11. Bubble capillary pressure evolution during Ostwald ripening in simulation 8 with two modified bubble layers at top and bottom (global equilibrium). The equilibrium indicator, F (in %), for the different images are: (a) 8.5, (b) 57.7, and (c) 91.1.

equilibrium follows the exponential theoretical model (Xu et al., 2017), characterized by a stagnant, yet uniformly decreasing bubble pressure gradient, while a dynamically and spatially changing bubble pressure gradient characterizes ripening in the global regime. Ripening in the global regime will occur when different regions in a porous medium contain bubbles with distinct pressures. Such conditions will typically occur in heterogeneous porous media and lead to slower ripening towards equilibrium than in homogeneous media (Mehmani and Xu, 2022a).

Table 6
Specifications of the mesh (Mesh_I – during imbibition and Mesh_R – during ripening) and control parameters V_{floor} and V_{th} [given in $(\Delta x)^3$] in the sandstone simulations.

Simulation	Mesh_I	Mesh_R	V_{floor}	V_{th}
CC_32_10	Uniform	Uniform	32	10
AC_32_10	AMR	Uniform	32	10
AA_256_10	AMR	AMR	256	10
AC_256_10	AMR	Uniform	256	10
AC_256_50	AMR	Uniform	256	50

6.2. Ripening post-imbibition in Castlegate sandstone

The last section revealed different generic behaviors of ripening kinetics for different spatial patterns of bubbles with low and high pressures constructed in a 2D homogeneous porous medium. However, the spatial bubble distribution depends on the prior displacement history of the fluids. Here we investigate the ripening of gas bubbles in sandstone using a capillary-trapped bubble configuration after imbibition. We use a sample of 3D Castlegate sandstone geometry with 200 × 200 × 200 grid cells and porosity 22.7%. The geometry is taken from a publicly available dataset with a voxel length of 5.6 μm (Sheppard and Prodanović, 2015).

We use the residual fluid configuration from previously published LS simulations of capillary-controlled primary drainage and imbibition with contact angle $\theta = 20°$ as starting point for the ripening investigation (Singh et al., 2023a; Helland et al., 2017). In primary drainage, gas invaded a completely water-filled sample from the bottom boundary ($z = 0$) by increasing the curvature P_c/σ stepwise, and in each step, Eq. (19) was solved to determine stationary states assuming continuous fluids with uniform capillary pressure (Helland et al., 2017). The subsequent imbibition, initiated from $S_w = 0.13$ after primary drainage, applied local volume conservation to the gas phase to handle gas bubbles that detached from the continuous phase (Singh et al., 2023a). In imbibition, the prescribed curvature between the continuous phases, P_c/σ, decreased stepwise. Water entered through the top boundary, and gas exited the bottom boundary as the side walls were sealed. The imbibition was terminated when all the remaining gas was capillary trapped as isolated ganglia. Two simulations of imbibition were run, one with a uniform coarse grid (*Uniform*) and the other with an adaptive grid having one level of refinement (*AMR*). Both simulations predicted the same residual gas saturation at the end of imbibition, $S_{gr} = 0.27$, but the different grid resolutions created slightly different imbibition paths, leading to slightly different residual gas configurations, see Fig. 12(a) and (b). In this section, we use the results from these two simulations as the initial state in ripening simulations to assess the impact of spatial bubble locations during ripening at constant gas saturation, as well as to investigate the effects of AMR and simulation control parameters in the ripening simulations.

The ripening investigations use CO_2 as the non-wetting phase, and the reservoir pressure and temperature are 15 MPa and 323.15 K. The CO_2-water phase properties are the same as in Section 5.1, except for the contact angle which is $\theta = 20°$. We use a constant mass transfer distance $\bar{l} = 81.06$ μm, which is a mean pore-channel length reported for Castlegate sandstone (Jiang et al., 2011). We use $\varepsilon = 0.05$ in Eq. (27). The characteristic parameters are set to $L^* = 5.6 \times 10^{-6}$ m and $\sigma^* = 10^{-4}$ N m^{-1}, which gives $P_c^* = 17.86$ Pa.

We carry out five simulations with different mesh resolutions and control parameters for volume thresholds, V_{floor} and V_{th} (see Table 6).

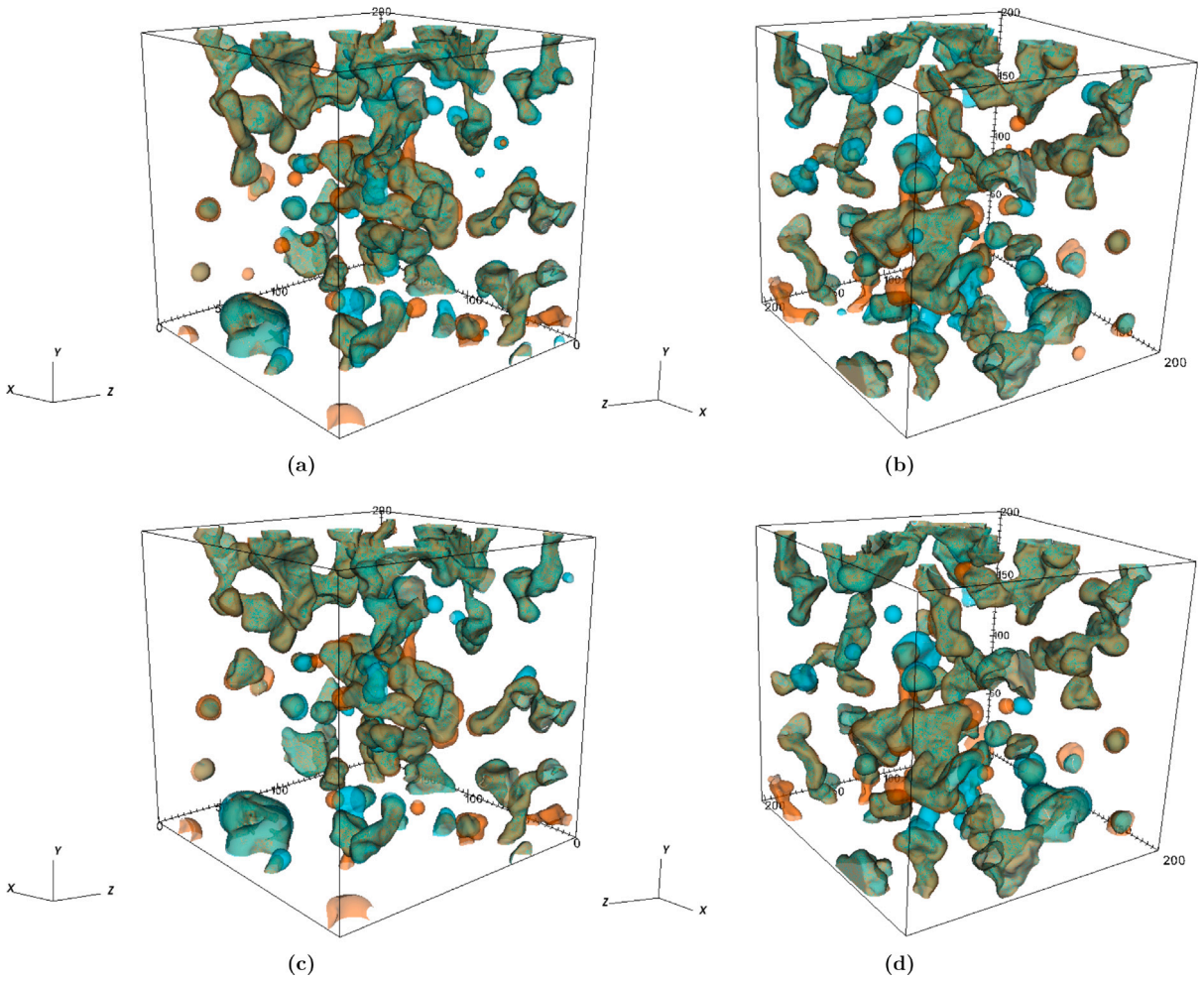

Fig. 12. Comparison of gas bubble locations from simulations in Castlegate sandstone. (a–b) Initial gas phase distribution for *AMR* (in *blue*) and *Uniform* (in *orange*) ripening simulations. (c–d) Comparison of ripening simulations *AC_32_10* (in *blue*) and *CC_32_10* (in *orange*) in Castlegate sandstone after 1.32 h. Images are from two diagonally opposite views.

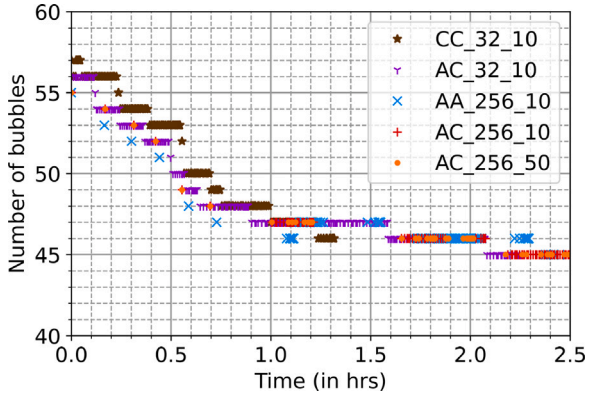

Fig. 13. Comparison of the number of gas bubbles during ripening in Castlegate sandstone. Simulation *CC_32_10* in *brown*, *AC_32_10* in *purple*, *AA_256_10* in *blue*, *AC_256_10* in *red*, and *AC_256_50* in *orange*. The simulations were run to different total times.

The simulations were terminated after at least 11 bubbles were lost from the system, which provided us with sufficient information to evaluate the impacts of the different parameters. Fig. 13 shows the initial and final number of gas bubbles during the evolution. Notably, the time scale of ripening for this CO_2-water case is faster than for the air–water case in Section 4 since for the same mass transfer lengths, the phase permeability of CO_2 in water at reservoir condition is nearly 10^4 times larger than that of air in water at atmospheric conditions. In the following sections, we discuss the simulation results in more detail (supporting information (Text S4 and Movie MS01) presents a video of the evolution from simulation *AA_256_10*).

6.2.1. *Different initial fluid distribution*

First, we discuss ripening simulations *CC_32_10* and *AC_32_10*, which have been run with the same mesh but slightly different initial bubble configurations caused by the different meshes used in the preceding imbibitions. Fig. 13 shows that the number of bubbles in the two simulations is generally different during evolution. Over time, the bubble numbers decrease in a similar manner, but there is a time lag between the bubble losses in the two simulations in the first hour. Fig. 12(c) and (d) shows the location of gas bubbles in the two simulations after 1.32 h. Among the bubbles with different initial locations in the two simulations, some remain in their positions while others have dissolved at 1.32 h. We plot the standard deviation in pressure, the average volume of bubbles, and the standard deviation in volumes in Fig. 14.

It is clear from these results that even though the two bubble configurations have similar gas saturation, their ripening paths are distinct. The number of bubbles and the average volume is the same at certain times, but the volume deviation remains different while the pressure deviation intersects at certain times. However, there are some common trends between the two simulations. The standard deviation

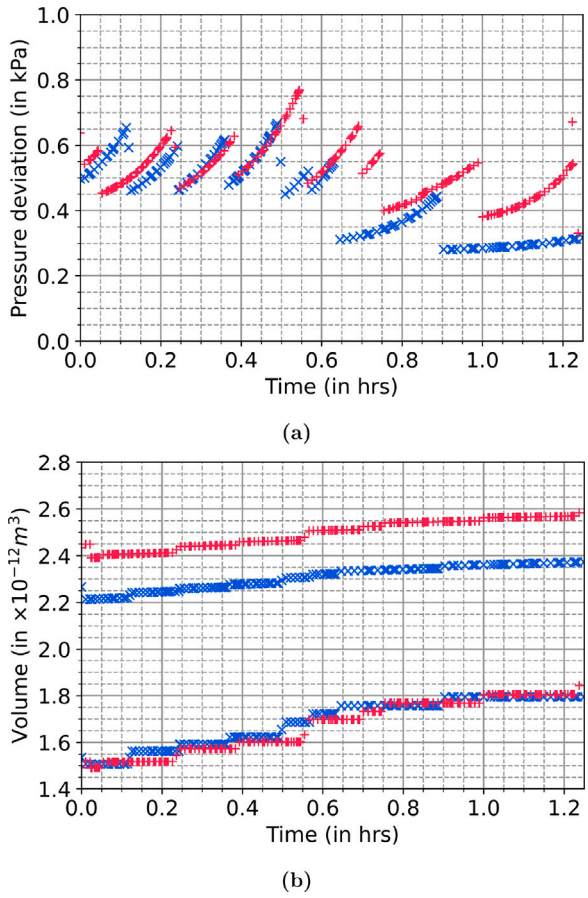

Fig. 14. Comparison of the ripening simulations *CC_32_10* (in *red*) and *AC_32_10* (in *blue*) in Castlegate sandstone. (a) Standard deviation in bubble pressures, and (b) standard deviation in bubble volumes (*top* two curves) and average bubble volumes (*bottom* two curves).

in pressure rises periodically, but overall the trend moves towards zero deviation. The pressure deviation rises cyclically since the bubbles losing mass decrease in size and often attain spherical shapes, which increases their pressure and leads to a rise in pressure deviation. This situation leads to the loss of bubbles from the system after some time, followed by a drop in the standard deviation of pressure since the bubbles with high pressures dissolved. Note that the pressure for the bubbles is calculated based on gas-liquid interface curvature in the pore space using the level-set method. The average volume of bubbles and the standard deviation in volume rises with noticeable staircase steps; each such step corresponds to a loss of bubbles from the system.

6.2.2. *Effect of mesh refinement and volume control parameters*

We perform one simulation of ripening with AMR (*AA_256_10*) on the residual bubble configuration from the AMR simulation of imbibition. The ripening simulation uses the same AMR and convergence specifications as the imbibition simulation (Singh et al., 2023a). We refine all grid cells in a band around the gas-water interfaces in the pore space, according to the criteria $|\phi| < \Delta x$ and $\psi > 0$. The refinement ratio is two, and regridding occurs every 2000 LS-iteration. Further, the error coefficient in Eq. (25) is $c = 5 \times 10^{-4}$, while reinitialization of ϕ occurs every 40 LS-iteration. We compare simulation *AA_256_10* against *AC_256_10*, which is its counterpart on a uniform coarse grid. Even though they start from the same initial state, Fig. 13 shows that the number of bubbles in the two simulations deviates early in the evolution. The simulation with refined mesh yields a lower number of bubbles in the system until a bubble splits at about 1.1 h and makes the number equal (see Figure S6 in Supplementary information). The average bubble volume also becomes approximately equal after this time (see Fig. 15(b)). Although the difference in volume is small after 1.1 h, the AMR simulation captures better the gas/liquid interfaces, which leads to higher accuracy in the calculation of bubble volumes and interfacial areas.

Table 7
Statistical parameters related to bubbles numbers (N), capillary pressure, and bubble volumes for the Castlegate simulations in Section 6.3 for the initial states and the states at 5.12 h. Average bubble volume (V_{av}), standard deviation (V_{std}), and total deviation U of bubble volumes are all in $\times 10^{-12}$ m^3. Average capillary pressure ($P_{c,av}$) and standard deviation in pressure ($P_{c,std}$) are in kPa.

Parameter	Initial		After 5.12 h	
	Sim1	Sim2	Sim1	Sim2
N	71	70	43	35
V_{av}	0.73	0.74	1.20	1.47
V_{std}	1.34	1.26	1.7	1.7
U	29.23	30	25.92	21.49
$P_{c,av}$	2.64	2.66	2.06	1.75
$P_{c,std}$	0.91	1.00	0.39	0.33

Figs. 13 and 15(b) suggest that the two simulations become similar after 1.1 h. However, Fig. 15(a) shows that the bubble pressure behaviors are different after this time, indicating that bubble losses occur at different times in the two simulations. Supplementary information (Text S3 and Figure S3) includes a comparison of the bubble configurations at 1.1 h and 2.25 h from the *AA_256_10* and *AC_256_10* simulations. In homogeneous media with identical pores, bubble volume, and pressure complement each other for bubbles limited to a single pore. But as the three plots highlight, in the complex pore geometry of porous rock, both pressure curves and volume curves are necessary to capture the ripening evolution.

In the numerical simulations, we assume different V_{floor} and V_{th} to control the physical time steps. Their value impacts the speed of computation as well as the possibility of numerical mass-transfer cyclicity in the simulation. Therefore, we compare scenarios where each of them has been changed individually to assess their impact on the ripening evolution results. Fig. 15(c) and (d) shows the comparison between simulations *AC_32_10* and *AC_256_10*. The curves are nearly overlapping. As expected, a higher V_{floor} skips data points for certain stationary states obtained with a lower V_{floor}. Supplementary information (Text S3 and Figure S4) compares gas bubble configurations from these simulations at 2.05 h. Fig. 15(e) and (f) shows a comparison between simulations *AC_256_10* and *AC_256_50*. These curves overlap completely. Although the time step is determined adaptively to manage cyclicity, the simulation with higher V_{th} allows larger time steps, and hence it omits certain stationary states observed in the simulation with a lower V_{th}. This difference did not lead to a deviation in the following evolution. Supplementary information (Text S3 and Figure S5) includes a comparison of gas bubble configurations from these two simulations after 2.4 h.

Higher values of V_{floor} and V_{th} improve the computational speed of the simulation at the risk of omitting major events from the evolution, such as a capillary instability that alters the behavior of the subsequent ripening. Among these two parameters, increasing V_{th} seems to give the least deviation in the results. Simulations with improved mesh resolution can predict a different ripening path, but AMR simulations are computationally expensive, so it might be prudent to use a higher V_{floor} or V_{th} when using adaptive mesh.

6.3. *Impact of gas bubble locations on ripening in Castlegate sandstone*

Here, we investigate ripening in two vastly different spatial bubble configurations that deviate much more than the two bubble configurations from the imbibition simulations with AMR and coarse uniform mesh in Section 6.2. For this purpose, we create two distinct bubble

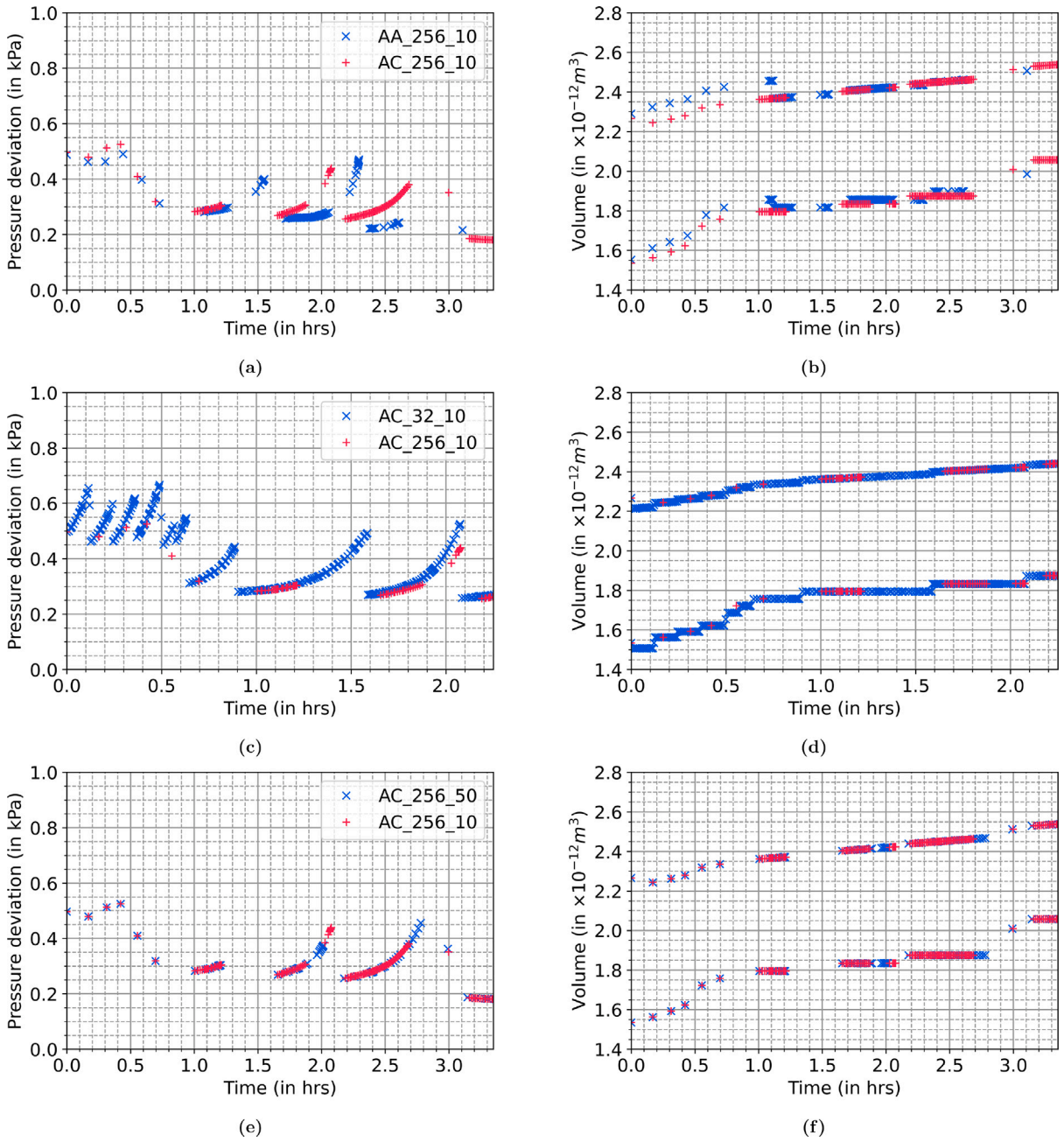

Fig. 15. Comparison of standard deviation in bubble pressures and volumes, and average bubble volumes, from different ripening simulations in Castlegate sandstone. (a–b) Different mesh resolutions, (c–d) different minimum bubble volume threshold, V_{floor}, and (e–f) different volume threshold for mass transfer, V_{th}. On the volume plots (b, d, f), the *top* two curves show standard deviation in bubble volumes, and *bottom* two show the average bubble volumes.

configurations by randomly populating CO_2 bubbles with different sizes on the Castlegate sandstone geometry (see Fig. 16(a) and (b)). We ensure that the bubble distributions are volumetrically similar, but the different locations of the bubbles affect the pressure variation in the distribution, even in the initial configuration before ripening (see Table 7). The gas saturation in the system is $S_g = 0.16$ in both cases. We run the ripening simulations on the coarse uniform mesh, using the volume control parameters $V_{th} = 20(\Delta x)^3$ and $V_{floor} = 32(\Delta x)^3$. All other parameters are the same as for the simulations on the coarse uniform mesh in the previous section. Supplementary information (Text S5, and Movies MS02 and MS03) presents a video of the ripening evolution for the two distributions.

Fig. 17(a) shows the evolution of gas bubble numbers in the two simulations (*Sim1* and *Sim2*). Although the two simulations start with nearly the same number of bubbles (70 and 71, see Table 7), the difference increases as the distributions ripen. In the final states (at 5.12 h), there are 43 bubbles (*Sim1*) and 35 bubbles (*Sim2*) left. In *Sim2*, there are two instances (at 1.2 h and 2.7 h) of a gas bubble splitting during the ripening, one due to mass gain and the other due to mass loss. The pressure deviation and volume deviation curves highlight the different ripening paths of the bubble configurations (see Fig. 17(b) and (c)). In the initial stage, the pressure deviation curve is more discontinuous since the time steps are larger, and each data point corresponds to the loss of a bubble. Fig. 16(a) and (b) shows that the fluid configuration in *Sim2* contained a larger number of smaller bubbles which are lost from the system in the first few time steps.

The average bubble volume increases at a faster rate in *Sim2* than in *Sim1*, and this rate difference is more significant after 1.7 h. Since gas saturation is constant, the rapid rise in average volume corresponds to a greater loss of bubbles from the system. An increase in the number

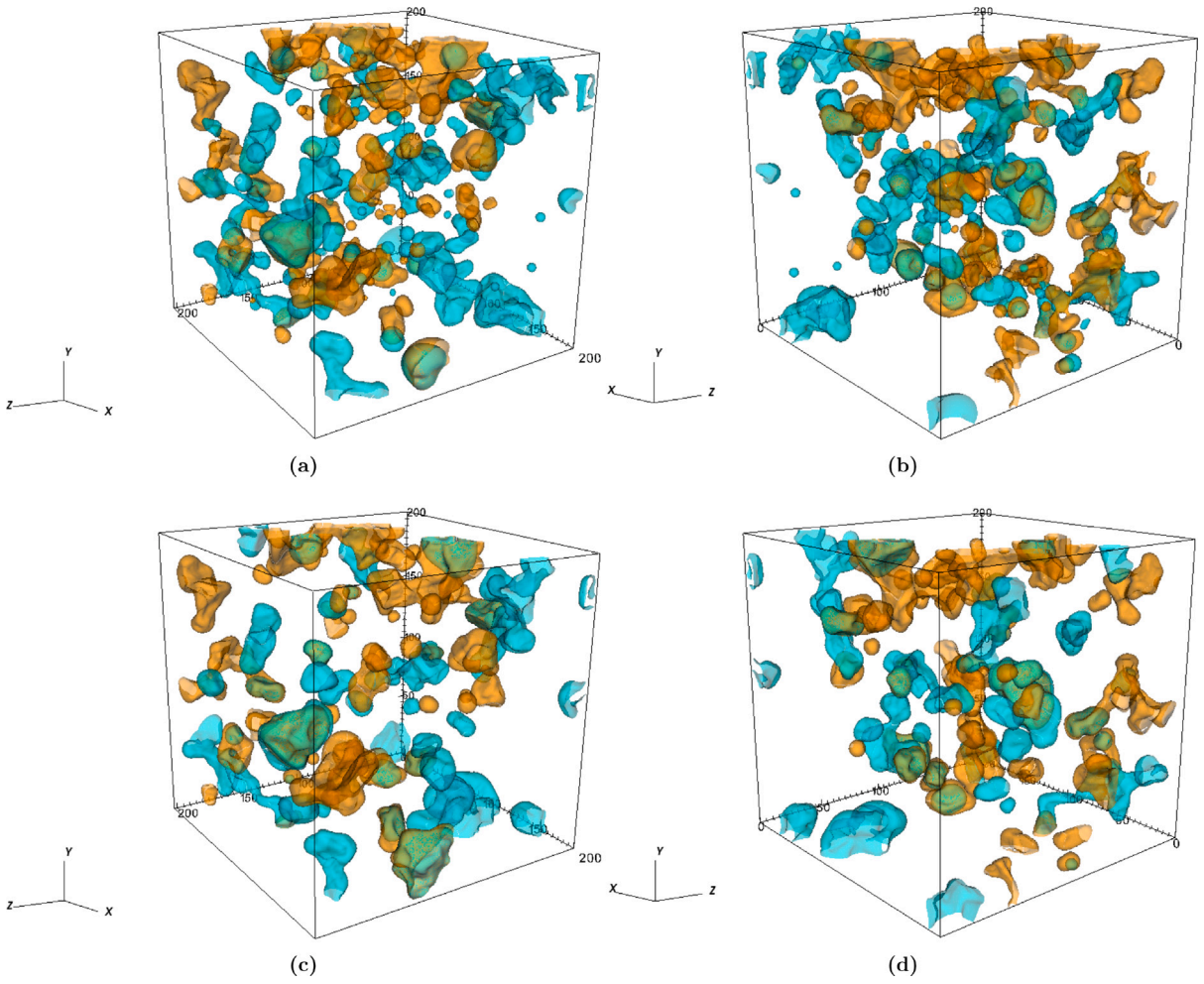

Fig. 16. Comparison of gas bubble locations from two simulations (*Sim1* and *Sim2*) of ripening in Castlegate sandstone with different initial gas bubble configurations. (a, b) Initial configurations, and (c, d) configurations after 5.12 h. Gas bubbles from *Sim1* are in *orange*, and gas bubbles from *Sim2* are in *blue*. The images show two diagonally opposite views.

of bubbles due to splitting also leads to a temporary decrease in the average bubble volume at two instances of time in *Sim2*. At 5.12 h, the fluid configuration in *Sim2* contains larger bubbles than that of *Sim1* (see Fig. 16(c) and (d)). Although the simulations terminated at 5.12 h, they suggest that at thermodynamic equilibrium, the number, volume, pressure, and spatial location of the bubbles will be different in the system (see Table 7).

7. Summary and conclusions

In this work, we have used a level-set based method to study Ostwald ripening of gas bubbles in arbitrary pore geometries that is compatible with parallel computations and adaptive mesh refinement. To model the mass transfer between gas bubbles, we considered both the ghost-bubble method (Singh et al., 2022) and a bubble-to-bubble method. We derived how the phase permeability coefficient of the gas in the liquid in the two methods relates to each other. Under simplified conditions with constant mass transfer areas and constant diffusive mass transport distance, we demonstrate that the two methods yield identical results. Then we used the bubble-to-bubble method in simulations of bubble ripening on a variety of geometries, including two pores separated by a pore throat, 2D and 3D homogeneous micromodel geometries, and a 3D sandstone geometry extracted from a micro-CT data set. Our aim was to investigate the impact of influential physical and numerical parameters on the ripening evolution.

We find that the pressure–volume behavior of bubbles (which depends on pore geometry) impacts both the time scale of the evolution and how the ripening evolves. Hence, the ripening behavior of two bubbles separated by a pore throat depends strongly on the converging/diverging shape of the pore throat walls as they determine the rate of change of bubble pressure with volume. On the other hand, the choice of mass transfer area for a diffusion path in the model (that is, minimum gas/water interface area or minimum cross-sectional pore-throat area) is important for determining the time scale of the ripening without significantly changing the nature of the evolution. Further, a comparison of experimental results from a micromodel with varying depth (Xu et al., 2017) against the results from ripening simulations on a similar geometry with a constant depth indicates that the discrepancy in evolution is caused by the differences in pressure–volume behavior and mass transfer area in the model due to the deviation in depths.

The ripening evolution in homogeneous media with identical pores depends on the spatial pattern of bubbles with high and low pressures in the initial configuration. Cases where each high-pressure bubble has a low-pressure bubble neighbor, yield a local ripening regime that follows an exponential curve as described by a theoretical model (Xu et al., 2017). However, ripening on bubble patterns with an increased spatial accumulation of bubbles with similar pressures will instead follow a slower, global ripening regime with sequential mass transfer through many bubbles. This behavior is not captured by the theoretical model. We find that a characteristic feature of the local regime is a stagnant bubble pressure gradient that decreases uniformly over time, while for the global regime, the pressure gradient changes dynamically with time and space.

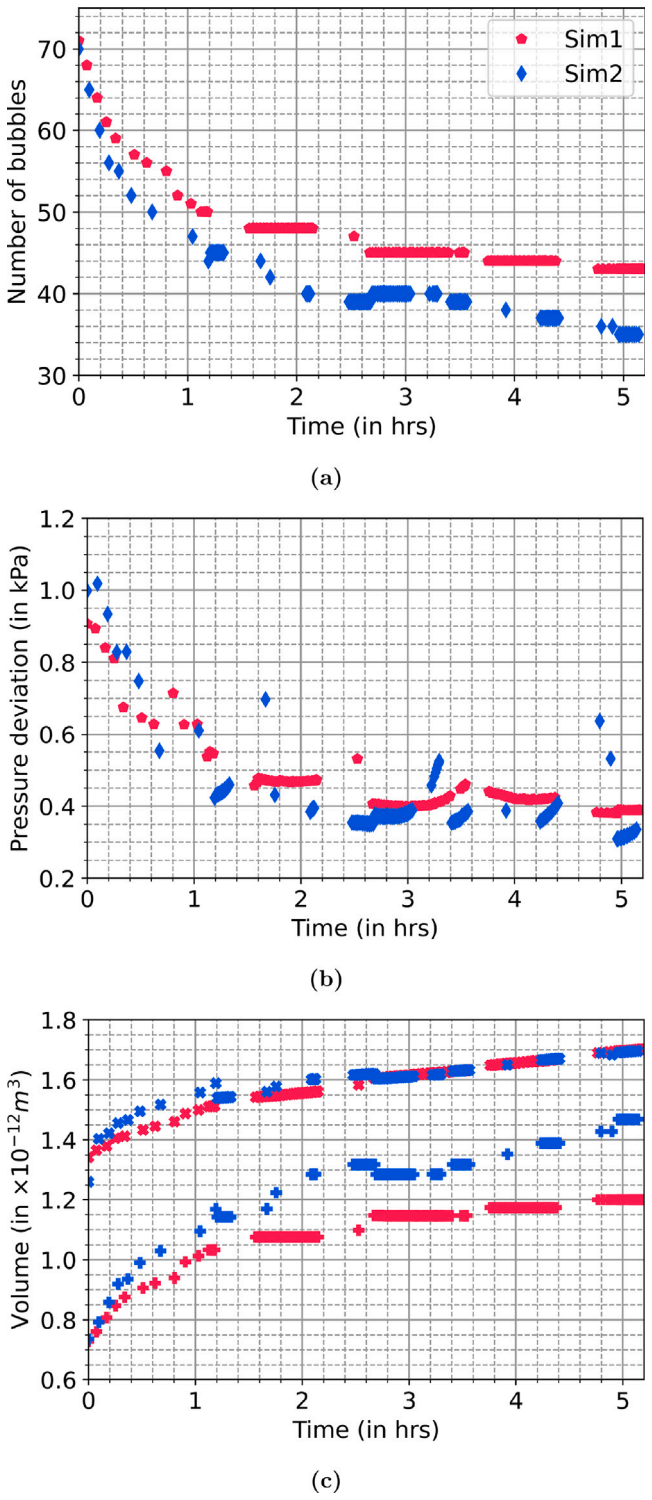

Fig. 17. Comparison of ripening from simulations with different spatial bubble distributions in Castlegate sandstone. (a) Number of gas bubbles, (b) standard deviation in bubble pressures, and (c) standard deviation in bubble volumes (*top* two curves) and average bubble volumes (*bottom* two curves).

Finally, simulations of bubble ripening on Castlegate sandstone show that increasing the mesh resolution on the imaged pore geometry can lead to slightly different evolutions over time in terms of bubble numbers, as well as pressure and volume behavior. We observed examples of bubbles that split due to both mass losses and mass gains, which demonstrates the complexity of the ripening behavior in these simulations. Different spatial bubble configurations in the sandstone with the same gas saturation ripen differently over time, and they do not end in similar states; instead, they develop different bubble numbers and different average bubble pressures and volumes.

At the field scale, both gravity and the capillary pressure gradient with depth impact the evolution of trapped gas bubble distributions. It has been predicted that ripening can lead to gas cap formation in around 10^5 years (Xu et al., 2019) or 10^6 years (Blunt, 2022). Singh et al. (2022) showed that the ripening of isolated bubbles in microfractured media leads to the enlargement of bubbles in microfractures, which can eventually mobilize trapped gas, reducing residual gas saturation. Consistent with other works (Xu et al., 2017; Moghadasi et al., 2023; Mehmani and Xu, 2022a), our results show that significant changes in capillary trapped gas-bubble configurations on the pore scale occur early in the ripening process. However, CO_2 storage projects where the lifetime of trapped CO_2 is a critical factor will benefit from conditions that lead to slower ripening times. Our results indicate that bedded or laminated subsurface reservoirs with different pore sizes in different layers could create such conditions in which the ripening occurs within the slow, global regime. A natural extension of this work is to explore three-phase (gas-oil-brine) ripening dynamics at different reservoir conditions, which can bring additional complexity and time scales to pore-scale bubble distribution evolution, which is relevant for CO_2 storage in depleted oil reservoirs.

CRediT authorship contribution statement

Deepak Singh: Conceptualization, Data curation, Formal analysis, Investigation, Methodology, Software, Validation, Visualization, Writing – original draft, Writing – review & editing. **Helmer André Friis:** Conceptualization, Data curation, Formal analysis, Investigation, Methodology, Software, Validation, Visualization, Writing – original draft, Writing – review & editing, Supervision. **Espen Jettestuen:** Conceptualization, Validation, Visualization, Writing – original draft, Writing – review & editing, Data curation, Formal analysis, Investigation, Methodology, Software, Supervision. **Johan Olav Helland:** Conceptualization, Data curation, Formal analysis, Funding acquisition, Methodology, Project administration, Resources, Software, Supervision, Validation, Writing – original draft, Investigation, Writing – review & editing, Visualization.

Declaration of competing interest

The authors declare that they have no known competing financial interests or personal relationships that could have appeared to influence the work reported in this paper.

Data availability

We have shared the link to our data at

Ostwald ripening of gas bubbles in porous media: Impact of pore geometry and spatial bubble distribution (Original data) (Figshare)

Acknowledgments

The financial support was provided by the Research Council of Norway through Petromaks2 project “Foam dynamics in the presence of oil during multiphase flow in porous rock (grant no. 294886)”. The computations were performed on resources provided by UNINETT Sigma2, the National Infrastructure for High Performance Computing and Data Storage in Norway.

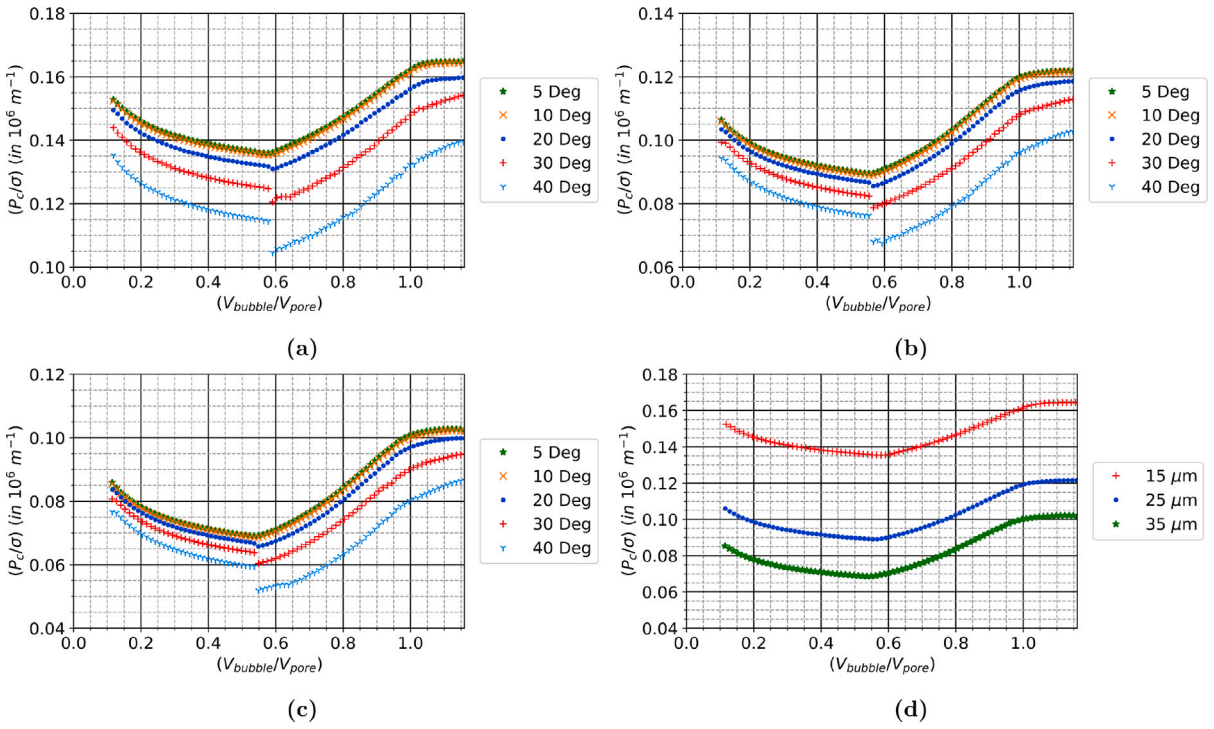

Fig. 18. Curvature vs. volume curve for the growth of a single bubble in a 3D micromodel pore with uniform depth. The graphs correspond to different depths and gas-liquid contact angles. (a) 15 μm depth, (b) 25 μm depth, (c) 35 μm depth, and (d) different depths for 10° gas-liquid contact angle. On the x-axis, the bubble volume is normalized by the volume of a single pore.

Appendix A. Interface curvature — bubble volume curve for different micromodel depths and contact angle

A key parameter in determining the rate of ripening is the volume rate of change in the capillary pressure as a bubble expands or shrinks in the pore space. In a micromodel geometry, the interface curvature at any location is a function of the contact angle and the depth of the micromodel.

Here, we use the LS model on a single pore of the micromodel geometry in Section 5.2 to simulate the relation between interface curvature $\kappa_0 = P_c/\sigma$ and bubble volume V_b for a series of increasing bubble sizes. For each specified gas bubble volume, we calculate the capillary pressure from Eq. (24) and solve Eq. (19) to a stationary state. We perform simulations for different micromodel depths and contact angles. The solid grains are cylindrical posts with a circular cross-section in the X–Y plane and depth along the Z-axis. In a 2D representation of this geometry, the largest inscribed circle will have a radius of 58.92 μm, and a volume fraction for minimum curvature, $V_{ci} = \left(V_b/V_p\right)_{\kappa_{min}} = 0.59$.

Fig. 18(a) shows the $\kappa_0(V_b)$-curve for different contact angles in the 3D geometry with 15 μm depth. The bubble grows to a minimum curvature until it contacts the solid phase (at $V_{ci} \approx 0.58 - 0.59$), and the curvature starts increasing again. The plots show several interesting features. As expected, the interface curvature decreases parabolically before the bubble contacts the solid grains, but these curves differ for different contact angles. This difference is due to the contact between the gas/liquid interface and the top/bottom solid surfaces. For smaller contact angles (5° and 10°), the contact with solid grains at V_{ci} leads to zero or negligible change in curvature, but with the increasing angle the curvature reduces progressively with the most noticeable change at 40° angle. This drop in curvature is due to a change in bubble shape in the circular cross-section in the X–Y plane once the bubble contacts the solid grains. In the case of smaller contact angles, the slope of the $\kappa_0(V_b)$-curve increases as the bubble moves farther into the pore throat, but after the bubble volume exceeds the pore volume, the slope of the curve decreases. In the case of larger contact angles, the curvature continues to increase beyond one pore volume while the slope of the curve remains relatively steep.

Fig. 18(b) and (c) show similar plots for 25 μm and 35 μm micromodel depth, for which the volume fraction V_{ci} is in the range 0.55–0.57 and 0.54–0.55, respectively. The plots highlight that both V_{ci} and κ_0 for different contact angles are functions of micromodel depth. Fig. 18(d) shows that the effect of depth on curvature reduces with increasing depth. Overall, Fig. 18 shows that the influence of contact angle on the interface curvature is less prominent with increased micromodel depth.

Appendix B. Supplementary data

Supplementary material related to this article can be found online at https://doi.org/10.1016/j.advwatres.2024.104688.

References

Ahmed, T., 2010. Vapor-lquid phase equilibria. In: Reservoir Engineering Handbook. Elsevier, pp. 1096–1234. http://dx.doi.org/10.1016/b978-1-85617-803-7.50023-7.

Anderson, R.W., Arrighi, W.J., Elliott, N.S., Gunney, B.T., Hornung, R.D., 2013. SAMRAI Concepts and Software Design. Technical Report LLNL-SM-617092-DRAFT, Livermore, CA, URL: https://computing.llnl.gov/sites/default/files/SAMRAI-Concepts_SoftwareDesign.pdf.

Attia, J.A., Kholi, S., Pilon, L., 2013. Scaling laws in steady-state aqueous foams including Ostwald ripening. Colloids Surf. A 436, 1000–1006. http://dx.doi.org/10.1016/j.colsurfa.2013.08.025.

Blunt, M.J., 2022. Ostwald ripening and gravitational equilibrium: Implications for long-term subsurface gas storage. Phys. Rev. E 106, 045103. http://dx.doi.org/10.1103/physreve.106.045103.

Cadogan, S.P., Maitland, G.C., Trusler, J.P.M., 2014. Diffusion Coefficients of CO_2 and N_2 in Water at Temperatures between 298.15 K and 423.15 K at Pressures up to 45 MPa. J. Chem. Eng. Data 59, 519–525. http://dx.doi.org/10.1021/je401008s.

Castellan, G., 1983. Physical Chemistry. Addison-Wesley, Reading, Mass.

de Chalendar, J.A., Garing, C., Benson, S.M., 2017. Pore-scale modelling of Ostwald ripening. J. Fluid Mech. 835, 363–392. http://dx.doi.org/10.1017/jfm.2017.720.

de Coninck, H., Revi, A., Babiker, M., Bertoldi, P., Buckeridge, M., Cartwright, A., Dong, W., Ford, J., Fuss, S., Hourcade, J., Ley, D., Mechler, R., Newman, P., Revokatova, A., Schultz, S., Steg, L., Sugiyama, T., 2018. Strengthening and implementing the global response. In: Masson-Delmotte, V., Zhai, P., Pörtner, H.O., Roberts, D., Skea, J., Shukla, P., Pirani, A., Moufouma-Okia, W., Péan, C., Pidcock, R., Connors, S., Matthews, J.B.R., Chen, Y., Zhou, X., Gomis, M.I., Lonnoy, E., Maycock, T., Tignor, M., Waterfield, T. (Eds.), Global Warming of 1.5 °C. An IPCC Special Report on the Impacts of Global Warming of 1.5 °C above Pre-Industrial Levels and Related Global Greenhouse Gas Emission Pathways, in the Context of Strengthening the Global Response To the Threat of Climate Change, Sustainable Development, and Efforts To Eradicate Poverty. Cambridge University Press, Cambridge, UK and New York, NY, USA, pp. 313–444. http://dx.doi.org/10.1017/9781009157940.006.

de Nevers, N., 2012. Appendix F: Calculation of fugacities from pressure-explicit EOSs. In: Physical and Chemical Equilibrium for Chemical Engineers. John Wiley & Sons, Inc., pp. 339–346. http://dx.doi.org/10.1002/9781118135341.app6.

de Vries, A.J., 1958. Foam stability: Part. II. Gas diffusion in foams. Recueil des Travaux Chimiques des Pays-Bas 77, 209–223. http://dx.doi.org/10.1002/recl.19580770302.

Farajzadeh, R., Vincent-Bonnieu, S., Bourada, N.B., 2014. Effect of gas permeability and solubility on foam. J. Soft Matter 2014, 1–7. http://dx.doi.org/10.1155/2014/145352.

Friis, H.A., Pedersen, J., Jettestuen, E., Helland, J.O., Prodanović, M., 2019. Pore-scale level set simulations of capillary-controlled displacement with adaptive mesh refinement. Transp. Porous Media 128, 123–151. http://dx.doi.org/10.1007/s11242-019-01238-6.

Helland, J.O., Friis, H.A., Jettestuen, E., Skjaeveland, S.M., 2017. Footprints of spontaneous fluid redistribution on capillary pressure in porous rock. Geophys. Res. Lett. 44, 4933–4943. http://dx.doi.org/10.1002/2017gl073442.

Helland, J.O., Pedersen, J., Friis, H.A., Jettestuen, E., 2019. A multiphase level set approach to motion of disconnected fluid ganglia during capillary-dominated three-phase flow in porous media: Numerical validation and applications. Chem. Eng. Sci. 203, 138–162. http://dx.doi.org/10.1016/j.ces.2019.03.060.

Hornung, R.D., Kohn, S.R., 2002. Managing application complexity in the SAMRAI object-oriented framework. Concurr. Comput.: Pract. Exper. 14, 347–368. http://dx.doi.org/10.1002/cpe.652.

Hornung, R.D., Wissink, A.M., Kohn, S.R., 2006. Managing complex data and geometry in parallel structured AMR applications. Eng. Comput. 22, 181–195. http://dx.doi.org/10.1007/s00366-006-0038-6.

Huppert, H.E., Neufeld, J.A., 2014. The fluid mechanics of carbon dioxide sequestration. Annu. Rev. Fluid Mech. 46, 255–272. http://dx.doi.org/10.1146/annurev-fluid-011212-140627.

Jettestuen, E., Friis, H.A., Helland, J.O., 2021. A locally conservative multiphase level set method for capillary-controlled displacements in porous media. J. Comput. Phys. 428, 109965. http://dx.doi.org/10.1016/j.jcp.2020.109965.

Jettestuen, E., Helland, J.O., Prodanović, M., 2013. A level set method for simulating capillary-controlled displacements at the pore scale with nonzero contact angles. Water Resour. Res. 49, 4645–4661. http://dx.doi.org/10.1002/wrcr.20334.

Jiang, Z., van Dijke, M.I.J., Wu, K., Couples, G.D., Sorbie, K.S., Ma, J., 2011. Stochastic pore network generation from 3D rock images. Transp. Porous Media 94, 571–593. http://dx.doi.org/10.1007/s11242-011-9792-z.

Kim, S.G., 2007. Large-scale three-dimensional simulation of Ostwald ripening. Acta Mater. 55, 6513–6525. http://dx.doi.org/10.1016/j.actamat.2007.07.058.

Krevor, S., Blunt, M.J., Benson, S.M., Pentland, C.H., Reynolds, C., Al-Menhali, A., Niu, B., 2015. Capillary trapping for geologic carbon dioxide storage – From pore scale physics to field scale implications. Int. J. Greenh. Gas Control 40, 221–237. http://dx.doi.org/10.1016/j.ijggc.2015.04.006.

Lemlich, R., 1978. Prediction of changes in bubble size distribution due to interbubble gas diffusion in foam. Ind. Eng. Chem. Fundam. 17, 89–93. http://dx.doi.org/10.1021/i160066a003.

Lemmon, E.W., Bell, I.H., Huber, M.L., McLinden, M.O., 1997. NIST Chemistry WebBook. NIST Standard Reference Database Number 69, National Institute of Standards and Technology, http://dx.doi.org/10.18434/T4D303, retrieved October 19 2022.

Li, Y., Garing, C., Benson, S.M., 2020. A continuum-scale representation of ostwald ripening in heterogeneous porous media. J. Fluid Mech. 889, A14. http://dx.doi.org/10.1017/jfm.2020.53.

Li, Y., Orr, F.M., Benson, S.M., 2021. Long-term redistribution of residual gas due to non-convective transport in the Aqueous phase. Transp. Porous Media 141, 231–253. http://dx.doi.org/10.1007/s11242-021-01722-y.

Lifshitz, I., Slyozov, V., 1961. The kinetics of precipitation from supersaturated solid solutions. J. Phys. Chem. Solids 19, 35–50. http://dx.doi.org/10.1016/0022-3697(61)90054-3.

Mehmani, Y., Xu, K., 2022a. Pore-network modeling of Ostwald ripening in porous media: How do trapped bubbles equilibrate? J. Comput. Phys. 457, 111041. http://dx.doi.org/10.1016/j.jcp.2022.111041.

Mehmani, Y., Xu, K., 2022b. Capillary equilibration of trapped ganglia in porous media: A pore-network modeling approach. Adv. Water Resour. 166, 104223. http://dx.doi.org/10.1016/j.advwatres.2022.104223.

Moghadasi, R., Goodarzi, S., Zhang, Y., Bijeljic, B., Blunt, M.J., Niemi, A., 2023. Pore-scale characterization of residual gas remobilization in CO_2 geological storage. Adv. Water Resour. 179, 104499. http://dx.doi.org/10.1016/j.advwatres.2023.104499.

Osher, S., Fedkiw, R., 2003. Level Set Methods and Dynamic Implicit Surfaces. Springer, New York.

Pentland, C.H., El-Maghraby, R., Iglauer, S., Blunt, M.J., 2011. Measurements of the capillary trapping of super-critical carbon dioxide in berea sandstone. Geophys. Res. Lett. 38, n/a. http://dx.doi.org/10.1029/2011gl046683.

Ranadive, A.Y., Lemlich, R., 1979. The effect of initial bubble size distribution on the interbubble gas diffusion in foam. J. Colloid Interface Sci. 70, 392–394. http://dx.doi.org/10.1016/0021-9797(79)90043-2.

Sander, R., 2015. Compilation of Henry's law constants (version 4.0) for water as solvent. Atmos. Chem. Phys. 15, 4399–4981. http://dx.doi.org/10.5194/acp-15-4399-2015.

Saye, R.I., Sethian, J.A., 2011. The Voronoi Implicit Interface Method for computing multiphase physics. Proc. Natl. Acad. Sci. 108, 19498–19503. http://dx.doi.org/10.1073/pnas.1111557108.

Sheppard, A., Prodanović, M., 2015. Network generation comparison forum. http://dx.doi.org/10.17612/P7059V, http://www.digitalrocksportal.org/projects/16.

Singh, D., Friis, H.A., Jettestuen, E., Helland, J.O., 2022. A level set approach to Ostwald ripening of trapped gas bubbles in porous media. Transp. Porous Media 145, 441–474. http://dx.doi.org/10.1007/s11242-022-01859-4.

Singh, D., Friis, H.A., Jettestuen, E., Helland, J.O., 2023a. Adaptive mesh refinement in locally conservative level set methods for multiphase fluid displacements in porous media. Comput. Geosci. 27, 707–736. http://dx.doi.org/10.1007/s10596-023-10219-0.

Singh, D., Friis, H.A., Jettestuen, E., Helland, J.O., 2023b. Pore-scale Ostwald ripening of gas bubbles in the presence of oil and water in porous media. J. Colloid Interface Sci. 647, 331–343. http://dx.doi.org/10.1016/j.jcis.2023.05.070.

Stevenson, P., 2010. Inter-bubble gas diffusion in liquid foam. Curr. Opin. Colloid Interface Sci. 15, 374–381. http://dx.doi.org/10.1016/j.cocis.2010.05.010.

Wang, C., Mehmani, Y., Xu, K., 2021. Capillary equilibrium of bubbles in porous media. Proc. Natl. Acad. Sci. USA 118, e2024069118. http://dx.doi.org/10.1073/pnas.2024069118.

Xu, T., Apps, J.A., Pruess, K., 2004. Numerical simulation of CO_2 disposal by mineral trapping in deep aquifers. Appl. Geochem. 19, 917–936. http://dx.doi.org/10.1016/j.apgeochem.2003.11.003.

Xu, K., Bonnecaze, R., Balhoff, M., 2017. Egalitarianism among bubbles in porous media: An ostwald ripening derived anticoarsening phenomenon. Phys. Rev. Lett. 119, 264502. http://dx.doi.org/10.1103/physrevlett.119.264502.

Xu, K., Mehmani, Y., Shang, L., Xiong, Q., 2019. Gravity-induced bubble ripening in porous media and its impact on capillary trapping stability. Geophys. Res. Lett. 46, 13804–13813. http://dx.doi.org/10.1029/2019gl085175.

Xue, Z., Worthen, A., Qajar, A., Robert, I., Bryant, S.L., Huh, C., Prodanović, M., Johnston, K.P., 2016. Viscosity and stability of ultra-high internal phase CO_2-in-water foams stabilized with surfactants and nanoparticles with or without polyelectrolytes. J. Colloid Interface Sci. 461, 383–395. http://dx.doi.org/10.1016/j.jcis.2015.08.031.

Yu, Y., Wang, C., Liu, J., Mao, S., Mehmani, Y., Xu, K., 2022. Bubble coarsening kinetics in porous media. Geophys. Res. Lett. 50, http://dx.doi.org/10.1029/2022gl100757, e2022GL100757.

Zhang, D., Song, J., 2014. Mechanisms for geological carbon sequestration. Procedia IUTAM 10, 319–327. http://dx.doi.org/10.1016/j.piutam.2014.01.027.